UNIVERSIDADE DE SÃO PAULO
INSTITUTO DE FÍSICA DE SÃO CARLOS

RENAN ARNON ROMANO

Evaluation of a portable multispectral fluorescence lifetime device for
skin cancer diagnosis using machine learning strategies

São Carlos
2020

RENAN ARNON ROMANO

Evaluation of a portable multispectral fluorescence lifetime device for skin cancer diagnosis using machine learning strategies

Thesis presented to the Graduate Program in Physics at the Instituto de Física de São Carlos, Universidade de São Paulo to obtain the degree of Doctor of Science.

Concentration area: Theoretical and Experimental Physics
Advisor: Profª. Drª. Cristina Kurachi

Corrected Version
(original version available on the Program Unit)

São Carlos
2020

With love,
to my parents, family
and wife.

ACKNOWLEDGMENTS

I would like to thank the "Macchu Picchu" fraternity friends for all the laughs, for kidding with Godofredo, and for cheering for me all the time, and for all the beers shared during my undergrad.

I would like to thank the "Amigos do Dória Metaleiro" Embrapa friends that since when I was an undergraduate research assistant are sharing laughs and jokes. Special thanks to Guto and Gaúcho, for the good friendship, advices, talks, coffees, and work.

I would like to thank the hard workers' women in science that contributed to this work, in the Jaú hospital, and in the cell studies.

Many thanks to Camilinha, Marlon, Dirceu, Ramon, and Thereza, for the friendship, for the great discussions, ideas, and code debugging. Special thanks to Ramon for all the help with the FLIm system. Special thanks to Dirceu for improving the thesis writing. Special thanks to Camilinha, who strongly resisted the daily likelihood to be transformed into a rubber duck, and helped me a lot with great ideas.

Many thanks for the USPSC SPIE Chapter for the leadership teachings, for the outreach activities that are so grateful.

Many thanks to the soccer and basketball teams for the friendship and the amazing games played together.

For all the infrastructure, without which this work would not be performed, many thanks to São Carlos Institute of Physics, to the CEPOF, to the people from the executive and financial boards, for all the secretaries, and for the graduate student service. Special thanks to the library service, Neusa, Sabrina and Cristina, for all the support during the thesis writing. Special thanks to Leandro from the mechanical atelier for all the help with the electric and mechanical of the FLIm system.

For the financial support, I would like to thank CAPES for the scholarship, and CEPOF, CNPq, and FAPESP for the lab infrastructure.

Finally, last but not least, I would like to thank my love, Hildegard. Many thanks for the daily support during the last three years. Many thanks for the great advices, for dreaming together, for inspiring me, for the daily routine from the "good morning" to the "good night", for all the joy, for the midnight talks and for the midnight laughs, for all the beers and parties shared on Sunday to Sunday, and, surely, for making me a better person.

Everyone mentioned in this acknowledgment makes me happier and more complete.Thanks all.

"The surest kind of knowledge is what you construct yourself"

Judea Pearl

ABSTRACT

ROMANO, R. A. **Evaluation of a portable multispectral fluorescence lifetime device for skin cancer diagnosis using machine learning strategies**. 2020. 104 p. Thesis (Doctor in Science) - Instituto de Física de São Carlos, Universidade de São Paulo, São Carlos, 2020.

Skin cancer diagnosis is a great challenge nowadays since it has the major incidence rates among all cancer types. Non-melanoma skin cancer is the most incident even being less aggressive, whereas melanoma is one of the most lethal cancer types due to its high metastatic potential. Early diagnosis is a main goal in new techniques development since it is responsible not only by increasing life expectancy, as well as decreasing treatment morbidity. Visual clinical inspection and then possibly dermoscopy and biopsy is the most common diagnosis procedure, being not so efficiently managed at the public health system, and can be very imprecise if not performed by a well-trained skilled dermatologist. An alternative early diagnosis technique is the label-free fluorescence since it is portable, real-time, non-invasive, not subjective, and that does not rely on exogenous fluorophores addiction. Some of the main native fluorophores are related to morpho-functional and metabolic activities on cells, thus, they can act as intrinsic optical biomarkers (OB), such as collagen, elastin, Nicotinamide Adenine Dinucleotide (NADH) and Flavin Adenine Dinucleotide (FAD). Since cancer causes mitochondrial dysfunction on cells, these molecules are powerful endogenous agents for diagnosis. In order to study the effect of cell's metabolic activities in autofluorescence, healthy fibroblasts cells, squamous cell carcinoma (SCC) and melanoma cancer cells were used. By two-photon excitation and multispectral steady-state and lifetime fluorescence microscopy, it was shown that optical redox ratio (ORR) and the lifetime parameters decrease in cancer cells, indicating that they may be relevant OB to distinguish cells. These OB were used in a clinical study on 119 patients with malignant lesions (melanoma, SCC, and nodular and superficial basal cell carcinoma (nBCC and sBCC)), and benign lesions (intradermal nevus (IN) and pigmented seborrheic keratosis (pSK)). Using a portable multispectral fluorescence lifetime imaging (FLIm) device, the patient skin cancer was imaged using a 355 nm excitation wavelength, and the fluorescence emission signal was detected in three channels mostly targeting collagen and elastin (390 ± 20 nm), NADH (452 ± 22 nm) and FAD (> 496 nm) emission. Using the OB extracted features, random forest, linear, and partial least square discriminant analysis classifiers were built on a training set and tested on a test set of images. As a result, to distinguish between healthy and nBCC tissue, classifiers showed that lifetime parameters are as important as steady-state fluorescence parameters, and achieved sensitivity of 88%. To distinguish between clinical similar malignant and benign lesions the models were tuned to achieve 100% sensitivity both on pigmented and non-pigmented lesions, which is very similar with the dermatologists' biopsy accuracy (87-94%). Two-way and five-way classification models achieved accuracies around 70% and 60%, whereas dermatologists accuracies is around 66% in this clinical diagnostic classification. In general, using the machine learning models, the FLIm technique was able to provide a fast and dermatologist-level skin cancer screening, which may contribute especially in areas where there is a lack of trained professionals.

Keywords: Fluorescence lifetime imaging. Skin cancer diagnosis. Machine learning.

RESUMO

ROMANO, R.A. **Avaliação de um sistema portátil multiespectral de tempo de vida de fluorescência para diagnóstico de câncer de pele utilizando aprendizado de máquina**. 2020. 104 p. Tese (Doutorado em Ciências) - Instituto de Física de São Carlos, Universidade de São Paulo, São Carlos, 2020.

O diagnóstico de câncer de pele é um grande desafio, pois este apresenta as maiores taxas de incidência entre todos os tipos de câncer. O câncer de pele não melanoma é o mais incidente, mesmo sendo menos agressivo, enquanto o melanoma é um dos tipos de câncer mais letais devido ao seu alto potencial metastático. A inspeção clínica visual seguida de dermatoscopia e possivelmente biópsia é o tipo mais comum de diagnóstico. Entretanto, este procedimento de não é de fácil adoção e gestão, além de ter baixa eficiência no sistema público de saúde, e pode ser impreciso se não for realizado por um dermatologista especialista treinado. Uma técnica alternativa de rastreio é a fluorescência sem marcador, por ser portátil, em tempo real, não invasiva e não depende da adição de fluoróforos exógenos. Alguns dos principais fluoróforos nativos estão relacionados às atividades morfo-funcionais e metabólicas das células, portanto, podem atuar como biomarcadores ópticos (BO) intrínsecos, tais como colágeno, elastina, dinucleotídeo de nicotinamida adenina (*NADH*) e dinucleotídeo de flavina adenina (*FAD*). Para estudar o efeito das atividades metabólicas na autofluorescência, foram utilizadas células saudáveis e cancerígenas. Por microscopia de estado estacionário e de tempo de vida de fluorescência, foi demonstrado que a razão óptica redox e o tempo de vida diminuem nas células cancerígenas, indicando que os BO são ideais para distinguir células. Neste contexto, os BO foram utilizados em um estudo clínico em 119 pacientes com lesões malignas (melanoma, carcinoma espinocelular e carcinoma basocelular (CBC)) e benignas (nevo intradérmico e queratose seborreica pigmentada). Usando um dispositivo portátil para aquisição de imagens de tempo de vida de fluorescência multiespectral (*FLIm*), o câncer de pele do paciente foi imageado usando uma excitação laser no comprimento de onda de 355 nm, e a emissão de fluorescência foi investigada em três canais: colágeno e elastina (390 ± 20 nm), *NADH* (452 ± 22 nm) e *FAD* (> 496 nm). Usando as características extraídas dos BO, os classificadores de floresta aleatória, análise de discriminante linear e de mínimos quadrados parciais foram construídos em um conjunto de treinamento e testados em um conjunto de imagens de teste. Para distinguir entre tecido saudável e CBC os classificadores mostraram que os parâmetros de tempo de vida são tão importantes quanto os parâmetros de fluorescência no estado estacionário e atingiram sensibilidade de 88%. Para distinguir entre lesões malignas e benignas clinicamente semelhantes, os modelos foram ajustados para alcançar 100% de sensibilidade nas lesões pigmentadas e não pigmentadas, o que é muito semelhante à precisão da biópsia dos dermatologistas (87-94%). Os modelos de classificação em duas e cinco vias alcançaram acurácia em torno de 70% e 60%, enquanto a precisão dos dermatologistas está em torno de 66% nesse tipo de tarefa. Em essência, usando os modelos de aprendizado de máquina, a técnica *FLIm* foi capaz de fornecer uma triagem rápida e em nível de dermatologista para o câncer de pele, o que pode contribuir especialmente em áreas onde há falta de profissionais treinados.

Palavras-chave: Imagem de tempo de vida de fluorescência. Diagnóstico de câncer de pele. Aprendizado de máquina.

LIST OF FIGURES

LIST OF TABLES

LIST OF ABBREVIATIONS AND ACRONYMS

ANSI	American National Standards Institute
AK	Actinic Keratosis
AUC	Area Under Curve
ANSI	American National Standards Institute
BCC	Basal Cell Carcinoma
CART	Classification and Regression Trees
CNN	Convolutional Neural Networks
DL	Deep Learning
DT	Decision Trees
FAD	Flavin Adenine Dinucleotide
FBS	Fetal Bovine Serum
FFT	Fast Fourier Transform
FLIm	multispectral Fluorescence Lifetime Imaging
FLIM	Fluorescence Lifetime Imaging Microscopy
FRET	Föster resonance energy transfer
FOV	Field of View
IN	Intradermal Nevus
KNN	K Nearest Neighbors
LDA	Linear Discriminant Analysis
MFLI	Macroscopic Fluorescence Lifetime Imaging
ML	Machine Learning
MLP	Multi-Layer Perceptron
MPE	Maximum Permissible Exposure
LR	Logistic Regression
NADH	Nicotinamide Adenine Dinucleotide
NMSC	Non Melanoma Skin Cancer
nBCC	nodular Basal Cell Carcinoma
OB	Optical Biomarker
ORR	Optical Redox Ratio
PLS-DA	Partial Least Squares – Discriminant Analysis

pSK   pigmented Seborrheic Keratosis

RF   Random Forest

ROC   Receiver Operator Characteristic

ROI   Region of Interest

sBCC   superficial Basal Cell Carcinoma

SCC   Squamous Cell Carcinoma

SPAD   Single-Photon Avalanche Diode

SVM   Support Vector Machine

TCSPC   Time-Correlated Single Photon Counting

LIST OF SYMBOLS

I_1	Integrated Intensity of FLIm Channel 1
I_2	Integrated Intensity of FLIm Channel 2
I_3	Integrated Intensity of FLIm Channel 3
$I_{n,1}$	Normalized Integrated Intensity of FLIm Channel 1
$I_{n,2}$	Normalized Integrated Intensity of FLIm Channel 2
$I_{n,3}$	Normalized Integrated Intensity of FLIm Channel 3
I_1/I_2	Ratio of Integrated Intensity of FLIm Channel 1 by Channel 2
I_2/I_3	Ratio of Integrated Intensity of FLIm Channel 1 by Channel 3
I_3/I_1	Ratio of Integrated Intensity of FLIm Channel 3 by Channel 1
$w_{slow,1}$	Slow lifetime weight of FLIm Channel 1
$w_{slow,2}$	Slow lifetime weight of FLIm Channel 2
$w_{slow,3}$	Slow lifetime weight of FLIm Channel 3
$\tau_{fast,1}$	Fast lifetime of FLIm Channel 1
$\tau_{fast,2}$	Fast lifetime of FLIm Channel 2
$\tau_{fast,3}$	Fast lifetime of FLIm Channel 3
$\tau_{slow,1}$	Slow lifetime of FLIm Channel 1
$\tau_{slow,2}$	Slow lifetime of FLIm Channel 2
$\tau_{slow,3}$	Slow lifetime of FLIm Channel 3
$\tau_{avg,1}$	Average lifetime of FLIm Channel 1
$\tau_{avg,2}$	Average lifetime of FLIm Channel 2
$\tau_{avg,3}$	Average lifetime of FLIm Channel 3

CONTENTS

1   INTRODUCTION

Cancer is a major public health problem, since it is the second cause of death worldwide and in Brazil.[1-2] An incidence of 600,000 new cases per year was estimated for 2018-2019, being 170,000 of non-melanoma skin cancer (NMSC), and 430,000 of other types of cancer. For every 100,000 people, it is estimated around 82 new cases of NMSC in the next two years. Although being the most prominent cause of cancer, NMSC is locally aggressive and not metastatic. On the other hand, with lower incidence (3 new cases in 100,000 people) melanoma skin cancer has a high mortality rate, being one of the most potentially metastatic cancer types.[2] In most cases, non-melanoma skin cancer has a full treatment response, while melanoma can present a good prognostics when treated at the initial stage, thus revealing how an early diagnosis is relevant.[1-2]

Based on changes in roughness, skin color, and superficial features, visual inspection is the most common method for skin cancer clinical diagnosis. Manual inspection (palpation), especially considering lesion adherence to deeper tissues, as well as detailed patient anamnesis are important additional information for diagnosis. When suspected features for lesion malignancy are detected, clinical diagnosis is followed by biopsy and histopathological analysis.[3-4]

In spite of clinical diagnosis being a fast procedure and, when performed by a well-trained dermatologist, well accurate, it still presents limitations. At initial stages, some lesions with distinct histopathological classes can be clinically similar, leading to misdiagnosis. Basal cell carcinoma (BCC) can easily be clinically classified as intradermal nevus (IN); squamous cell carcinoma (SCC) is clinically similar to actinic keratosis (AK), while the most lethal misdiagnosis is between melanoma and pigmented seborrheic keratosis (pSK).[5-8] Different pathologies have distinct treatment procedures, and a misdiagnosis will result in important consequences, especially for the cancer patients. Another limitation of the clinical diagnosis is the difficulty in determining the tumor borders during the lesion excision, leading to an incomplete excision rate that can be as high as ~65%.[3-4, 9] Again, the consequences of a failed detection will result in higher rates of morbidity and, mostly, in the case of melanoma, higher mortality.

Aiming to improve diagnosis, optical methods coupled with computational analysis and classification algorithms have shown great potential.[10-14] Optical techniques are attractive since they have, in general, low cost and portable instrumentation, besides being able to provide real-

time feedback through a non-invasive and non-destructive *in situ* procedure. Additionally, computational analysis can be very fast with the recent advances in the hardware, and highly accurate on finding patterns with the great potential of artificial intelligence. Among optical-based techniques, fluorescence is one of the most convenient chosen light-tissue interaction, since the information from endogenous and exogenous fluorophores can be useful for distinguishing healthy from diseased tissues, as well as being a tool for interrogating tissue response during a wide range of treatments.[15-19]

Fluorescence optical diagnosis was frequently called "optical biopsy"; however, it does not require tissue sample excision as the conventional biopsy, so constituting a non-invasive diagnosis technique. Label-free fluorescence is a technique in the optical diagnosis field, when this method uses tissue native fluorescence information to distinguish tissue conditions, not requiring the introduction of any exogenous biomarker.[20-21] In this context, two coenzymes of cellular metabolism gain prominence: Nicotinamide Adenine Dinucleotide (NADH) and Flavin Adenine Dinucleotide (FAD), not only by their functional main role but also for their diagnostic potential as native optical biomarkers.[21]

NADH and FAD are involved in a wide range of mitochondrial functions, such as calcium homeostasis, gene expression, oxidative stress, aging, and apoptosis. Mitochondrial metabolism is responsible for all the chemical processes for energetic transformations that are essential to the life of all eukaryotic cells and human health. Mitochondria undergoes support for energy demands for all cellular processes and cell proliferation, being also responsible for programmed cell death, free radical generation, as well as oxidative stress and biomolecular sensing of glucose. Hence, mitochondrial dysfunction and anomalies dysregulate energy production as well as dysregulates many pathways of intermediary metabolism. As a result, it is linked to a wide range of diseases such as neurodegenerative diseases (Alzheimer, Parkinson, and Huntington), diabetes, and cancer.[22-24] NADH and FAD present differences in their amount and bound or free states due to metabolic changes, being main fluorescent markers to track mitochondrial dysfunction. Besides these two, tryptophan, collagen and elastin are also widely studied endogenous fluorophores, presenting characteristics of changing their conformation and amount in disease tissue, especially related to cancer progression.[25]

In this study, a strategy for screening cutaneous cancer using skin autofluorescence is presented. A portable fluorescence lifetime device is evaluated aiming to discriminate healthy and abnormal tissues, including the classification in three types of skin cancer and two benign tissue conditions. The following sections present the state-of-the-art of the optical diagnosis, a

theoretical review for the principles of the study, the methodology, and the achieved results and conclusions.

2 LITERATURE REVIEW

2.1 Skin cancer

Skin cancer is the most incident cancer type, and it is mainly caused by UV sunlight prolonged and continuous exposure. Its occurrence in the general population, however, is dependent mainly on the basis of skin complexion and can vary according to hereditary factors. They can be divided into two categories: NMSC, which comprises both BCC and SCC, and melanoma skin cancer. Considering all skin cancers, incidence rates are of 80 % of BCCs, 16% of SCCs, and 4% of melanomas.[8, 26-27]

BCC is a malignant neoplasm developed in the basal cells, which are present in the lowest layer of skin epidermis. BCC growth rate is slow, presenting higher incidence at the face, neck, scalp, lower arms and hands, body regions that have higher sunlight exposure. The lesion usually appears as pearls with rolled borders, but it also can appear without satisfactory border delineation. Thus, it can be similar to intradermal nevus, a type of benign skin condition. Metastasis is rare in this type of cancer, but they tend to cause morbidity, especially when the lesions are in the head and neck regions.[8, 27]

SCC is the second most common skin cancer, as well as BCC they usually occur on sun-exposed sites, and mostly develops on the dry and rough parts of the skin. Usually, they appear in the form of red or blackish yellow spots. It grows faster than BCC, most of the cases do not show high aggressiveness, but it already presents a small risk of metastasis (around 4 %).[8, 26-27]

Melanoma is less common than BCC and SCC, however, it is very aggressive, and it is highly lethal if not diagnosed at early stages. The major part of deaths related to skin cancer is caused by melanomas (75%). It develops mostly from the melanocytes at the epidermal layer, but may also originate from the dermal layer. Lesion appearance is the basis of the clinical screening and diagnosis, and usually, it is asymmetric (A), with no clear borders (B), and has different colors (C) within the lesion, diameter (D) greater than 6 mm, and a fast evolving (E) pattern. Verifying these five clinical features is known as the ABCDE rule for melanoma screening. However, pSK, a benign skin condition, can have the same properties in the ABCDE rule, leading to an incorrect diagnosis. A misled melanoma diagnosis can cause patient death.[6, 8, 27-28]

Skin cancer diagnosis is based on clinical visual inspection, with or without a dermoscopy visualization, which can be followed by a biopsy. For NMSC, clinical and physical evaluation sensitivity varies from 56 to 90%, while specificity ranges from 75 to 90%, whereas

biopsy techniques improve sensitivity up to 94 to 99%, and specificity up to 80 to 91%. Despite biopsy techniques shows higher scores, it is not usually performed due to the low aggressiveness of these types of cancer.[5] For melanoma, biopsy techniques are always performed (when it is available) and have diagnostic accuracies of 95 to 99%.[6] In some cases, due to the incorrect clinical diagnosis of malignant lesions, biopsies and histopathology analyses are not performed, leading to harmful patient outcomes.

Despite the high diagnostic precision achieved by dermoscopy and biopsies, these techniques require trained and skilled dermatologists and pathologists. However, Brazil's distribution of dermatologists is very unequal country wise as shown in a recent study by Buzzá et al.[29] For dermatologists by a thousand of inhabitants, it reported values ranging from 1.16 to 2.81, for the poorest and richest regions respectively. The unequal distribution reflects directly on the diagnosis and treatment, leading to more sub-diagnosed skin conditions in regions with a lack of dermatologists. Thus, auxiliary tools for clinical diagnosis and screening of skin cancer are still needed.

2.2 Label-free fluorescence studies

Since the last years of the 1980s decade and early years of the 1990s decade, several studies have been conducted exploring endogenous and exogenous fluorescence under UV excitation. Studies were performed in a wide variety of target tissues, such as liver, lung, oral mucosa, cervix, esophagus, kidney, breast, and brain. These studies showed great potential for spectroscopy of endogenous fluorophores under UV excitation for both *in vivo* and *in vitro* interrogation, and comparing healthy and abnormal tissues or cells.[30-35] Since these techniques showed diagnostic potential, one approach used to improve their feasibility was to use multiple wavelength excitation and acquisition. Using this approach, studies were able to detect changes mostly in the ratio of NAD+/NADH (redox ratio), which is a metabolic marker for mitochondrial abnormalities, and blood oxidation states. Together, these studies showed that NADH, FAD, collagen, elastin, keratin, and tryptophan are the main relevant biomarkers for detecting correlations between spectral signatures and tissue pathologies,[25] and paved the way for present studies.

Recently, endogenous fluorescence studies range from *in vitro* to *in vivo* and *ex vivo*, from spectroscopy to imaging techniques, and from steady-state to time-dependent fluorescence. A complete study on metabolic changes was done by Liu Z. *et al.*,[23] in which NADH and FAD were mapped both *in vivo*, *in vitro* and *ex vivo* by employing two-photon

excited steady-state and lifetime fluorescence. A wide number of experiments are presented in human keratinocytes, C2C12 myoblasts, HL-1 cardiomyocytes, and mesenchymal cells, as well as brown adipose tissue for both *in vivo* and *ex vivo* experiments. This study reports reduction of redox ratio during conditions of hypoxia, cell supplementation of free fatty acids (oleate and palmitate) and adipogenic differentiation, whereas an increase of redox ratio was observed under glucose starvation, chemical uncoupling, and cold activation. The same type of experiments was performed while looking at the bound fraction of NADH and mitochondrial clustering and results are complementary.[23]

Pouli *et al.*[24] imaged mitochondrial dynamics in human skin by two-photon excitation of NADH and FAD both *in vitro* and *in vivo*, revealing depth-dependent hypoxia and then the potential for malignant diagnosis. The analysis of steady-state and lifetime fluorescence led to different values of mitochondrial clustering during normoxia and hypoxia. Thus, a classification using cross-validation analysis resulted in a precision of 89% of the cases (100% specificity and 82% sensitivity). In addition, another study of multiphoton imaging of mitochondrial optical redox ratio was also able to identify metastatic potential in breast cancer cells,[36] showing an increase of metastatic potential with the increase of the redox ratio under normoxia.

Föster resonance energy transfer (FRET) studies using endogenous fluorophores were also reported in the literature. FRET is a type of non-radiative energy transfer between two molecules, the donor which will be excited and donate its energy, and the acceptor molecule, which will receive the energy. FRET occurs when the donor molecule fluorescence emission band and the acceptor molecule absorption band have similar wavelengths range. FRET efficiency is used as a measurement of the molecules' proximity and interaction.[37] Recently, tryptophan and NADH interactions were investigated by Jyothikumar *et al.*,[38] detecting FRET between these fluorophores under three-photon excitation. FRET efficiency decreased for HeLa cells under glucose starvation, opening a field of study of quenching patterns in different pathologies.

FRET between NADH and FAD was also observed by fluorescence spectroscopy in *ex vivo* mice brain tissue by Shi L. *et al.*,[22] which employed UV excitation and monitored the endogenous coenzymes and tryptophan. As a result, it was possible to discriminate tissues of Alzheimer's Disease in animal models. Both fluorescence intensity of all fluorophores and FRET efficiency were higher in the Alzheimer's disease tissue when compared to normal.

Steady-state and lifetime spectroscopy of endogenous fluorophores techniques have focused on biological analytes, whereas imaging techniques found their way in the molecular imaging field. Although these research activities had a great impact on the label-free

fluorescence field, techniques adapted for *in vivo* and clinical studies were still an open challenge in fluorescence lifetime research.

2.3 Fluorescence lifetime imaging systems

Distinct fluorescence lifetime imaging microscopy (FLIM) instrumentations for *in vivo* measurements were already assembled. Sinsuebphon *et al.*[39] built a macroscopic fluorescence lifetime image (MFLI) device to quantify FRET for *in vitro* and *in vivo* in animal models. They used an IR wavelength laser to excite samples of the inguinal mammary fat pad by two-photon absorption. Exogenous fluorophores Alexa Fluor 700 and 750 were also used for *in vitro* imaging. Miller *et al.*[13] built a system for both endogenous and exogenous fluorescence acquisition to study skin cancer lesions in a pre-clinical study. Five (n=5) female athymic nude mice had 10^6 cells of SCC intradermally injected, and tumors were allowed to grow for 3 weeks before imaging. For autofluorescence, lasers emitting at 480 and 535 nm were used, whereas for exogenous fluorescence excitation lasers at 785 and 820 nm were employed. Endogenous fluorescence lifetime results indicate that NADH and FAD lifetimes were shorter in SCC lesions than in healthy surrounding tissue.

A wide-field FLIM was presented by McGinty *et al.*[40] using 355 nm laser for the excitation of *ex vivo* samples of SCC, liver containing metastatic colorectal carcinoma, pancreatic cancer and gastrectomy adenocarcinoma. Although this system has a single channel, i.e., different fluorescence spectral ranges are not separated during acquisition, results showed differences in all tissue fluorescence lifetime measurements.

Advances in the detection systems enable the assembling of other devices targeting label-free interrogation, featuring either three or four spectral channels acquiring emission of several combination of endogenous fluorophores at the spectral ranges of 300-350 nm; 350-430 nm; 430-500 nm; 500-600 nm and 600-700 nm, mainly related to Tryptophan, Collagen/Elastin, NADH, FAD, and Porphyrins respectively. Shrestha *et al.*[41] built a table-top multispectral fluorescence lifetime imaging (FLIm) system for pre-clinical applications employing a 355 nm laser and targeting fluorescence detection from collagen, NADH, and FAD (390 ± 20 nm, 452 ± 22.5 nm, 550 ± 20 nm respectively). The system was successfully employed on imaging of lesions from hamster oral dysplasia, demonstrating that the technique is able to distinguish malignant and healthy tissues. Using the same laser for excitation and acquiring signals from the same emission bands, another similar system built by Park *et al.*[42] was used for the biochemical characterization of *ex vivo* coronary atherosclerotic plaques. This report

demonstrated that the steady-state and lifetime signals are highly sensitive for discriminating regions with higher and lower amounts of collagen and lipids, showing other types of application for similar systems.

Bec *et al.*[43] imaged fluorescence lifetime using UV excitation at 355 nm. They investigated the *in vivo* structural and biochemical features of coronary arteries in a swine model with an intravascular catheter. Fluorescence was split into four channels at 390 ± 40 nm, 452 ± 45 nm, 542 ± 50 nm, and 629 ± 53 nm for observing collagen, elastin, lipoproteins, and ceroid, respectively.

Furthermore, Sun *et al.*[44] and Cheng *et al.*[45-46] reported FLIm systems, which were built based on two approaches. The first approach featured a flexible, coherent fiber bundle-based endoscope, whereas the second one involved a handheld probe. Both approaches were used for *in vivo* imaging, exciting the samples using 355 nm laser light, and being able to allow the acquisition of the fluorescence emission bands of 390 ± 20 nm, 452 ± 22.5 nm, and > 550 nm, mainly related to collagen/elastin, NADH and FAD respectively. First, they were applied to study hamster's cheek pouch, allowing to detect dysplasic lesions, [45] then on *ex vivo* human oral biopsy and *in vivo* ventral region of one volunteer human tongue. More recently, a report from a clinical *in vivo* application of the same system evaluating twenty patients with oral epithelial cancer was published.[46] This report demonstrates that this type of system has potential for distinguish between healthy and malignant oral tissues. However, due to the lower number of patients imaged, there are no mentions about the classification scores such as precision, specificity and sensitivity.

Evaluation of skin lesions by fluorescence lifetime systems has also been reported in the literature. De Beule *et al.*[17] showed the development of a hyperspectral fluorescence lifetime device that uses two ultrafast lasers emitting at 355 and 440 nm and acquire fluorescence lifetimes ranging from 390 to 600 nm (with resolution of 15 nm). Results of evaluating eighteen (18) fresh *ex vivo* biopsies of human skin lesions indicate that such technique can be used on the discrimination of BCC lesions from healthy tissues, and results for NADH and FAD lifetimes also correlates with Miller *et al.*,[13] who showed shorter lifetimes for both fluorophores in lesion region comparing with surrounding tissue. Using 355 nm laser for autofluorescence excitation and only one channel of acquisition (>375 nm) Galletly *et al.*[18] also performed FLIM measurements of twenty-five *ex vivo* fresh biopsies of human BCC skin cancer. The reported results indicate that lifetime decays extracted from this technique can help on the detection and delineation of the borders of human BCC, however, when the average value of autofluorescence intensity was observed, no significant differences were found. Furthermore, an animal study

using forty-two mice by Pires *et al.*[47] used two pulsed lasers (378 and 445 nm) for exciting melanoma *in vivo*. Acquiring signals mainly related to NADH and FAD on the emission bands of 440 ± 40 nm and 514 ± 30 nm respectively, the study reports accuracies up to 94% on distinguish melanoma from healthy tissue. Moreover, melanomas associated lifetime values showed to be higher when compared to normal tissue.

Although there is a high number of studies showing FLIM diagnostic potential, there is still a lack of clinical studies analyzing a high number of patients and lesions. It occurs, in general, due to the difficulties to develop a portable, safe (due to the low intensity of the UV light), and user-friendly device that could feasibly be incorporated during the routine clinical procedures. Table 2.1 summarizes the main features of the FLIM studies presenting instrumentation development and its use.

Table 2.1 - Summary of main features of the fluorescence lifetime imaging systems studies.

Author	Fluorophore type	Tissue type	Tissue	Laser source (*/nm)
Sinsuebphon *et al.*[39]	Exogenous – Alexa Fluor 700 and 750	Mouse mammary fat pad	*in vivo*	2 p* – 695
Miller *et al.*[13]	Endogenous – NADH and FAD and Exogenous – Cyapate-GRD	Mice SCC skin cancer	*in vivo*	1p* – 480/535 2p* – 785/820
McGinty *et al.*[40]	Endogenous – NADH FAD Keratin all	Human biopsy of colon, stomach, bladder, liver, and pancreas	*ex vivo*	1p* – 355
Shrestha *et al.*[41]	Endogenous – Collagen, Elastin NADH and FAD	Hamster oral dysplasia	*in vivo*	1p* – 355
Cheng *et al.* [45, 46, 48]	Endogenous – Collagen, Elastin NADH and FAD	Human oral dysplasia	*in vivo*	1p* – 355
Park *et al.*[42]	Endogenous – Collagen, Elastin NADH and FAD	Human segments of coronary plaques	*ex vivo*	1p* – 355
Bec *et al.*[43]	Endogenous – Collagen , Elastin, lipoproteins and ceroid	Swine coronary arteries	*in vivo*	1p* – 355
De Beule *et al.*[17]	Endogenous – Keratin, collagen, NADH, and FAD	Human Skin cancer biopsies	*ex vivo*	1p* – 355/440
Galletly *et al.*[18]	Endogenous – NADH and FAD	BCC human biopsy Skin cancer	*ex vivo*	1p *– 355

* 1p and 2p refers to 1 photon and 2 photon excitation, respectively
Source: By the author.

2.4 Computer-aided diagnosis of skin lesions

The potential of computer-aided decisions for diagnosis of skin lesions has been demonstrated since the early 1990s.[49] Until the early 2010s, it has been described as a powerful support tool for physicians having accuracy levels similar to trained dermatologists.[50-51] However, nowadays, with the advances in computational power, and the generation of massive and high-quality data, these techniques show a possibility to achieve even higher accuracy than highly experienced and skilled dermatologists.[52]

Pattern recognition methods for skin lesion diagnosis have already been demonstrated as powerful classification tools. Several types of optical techniques were used: digital photography, dermoscopy, multispectral imaging, fiberoptic spectroscopy, confocal microscopy, multispectral lifetime and steady-state microscopy and macroscopy, optical coherence tomography and others.[51] The reported studies used several classification methods such as linear discriminant analysis (LDA), support vector machines (SVM), K nearest neighbors (KNN), decision trees (DT), logistic regression (LR), multi-layer perceptron (MLP), deep learning (DL) on convolutional neural networks (CNN), among others. [5, 18, 50-53] Table 2.2 shows some selected studies of computer-aided diagnosis of skin lesions, summarizing the dataset size, methods, and accuracies achieved by the optical technique used.

Table 2.2 - Summary of selected studies of computer-aided diagnosis of skin lesions.

Author	Optical technique	Dataset size (number of samples)	Method	Accuracy (%)	Year
Schindewolf et al.[49]	Slide images	350	CART	92	1993
Burroni et al.[50]	Dermoscopy	840	KNN	95	2004
Galletly et al.[18]	Fluorescence lifetime on slides	24	LDA	95	2008
Premaladha et al.[53]	Dermoscopy	992	CNN (DL)	93	2016
Esteva et al.[52]	Digital Photography and dermoscopy	$1.6.10^6$	CNN (DL)	72	2017

Source: By the author.

The selected studies reported dermatologist level accuracy with higher levels (80 – 96%) of sensitivity and specificity. However, it is important to observe the differences in the optical

techniques, dataset and accuracy achieved. The study by Schindewolf *et al.*[49] in 1996 was the first attempt to distinguish skin cancer, with a medium-sized dataset (350 tissue slide images), achieving a 92% of accuracy. Despite the higher accuracy level, it was still based on the lesion excision, tissue processing and further a complete scanning of the slide and analysis, providing automation of the pathology evaluation but not being able to perform *in situ* diagnosis. In the following years, aiming to increase dataset size, studies focused on simpler optical imaging techniques, such as photography and dermoscopy. Studies using dermoscopy images increased dataset size to around one thousand samples.[50, 53] The authors were able to achieve accuracies around 95% and sensitivity of 98%. These studies used both simple methods such as LDA and KNN,[50] as well as a powerful method of CNN (DL).[53]

Although the increase in the dataset size led to an increase in the accuracy and sensitivity scores, a recent study with a huge dataset of 1.6 million biopsy-proven skin cancer images, divided into inflammatories, geodermatities, benign-dermal, benign-epidermal, benign-melanocytic, malignant-dermal, malignant-epidermal, malignant-melanoma, and malignant-cutaneous lymphoma, showed a decrease in the overall accuracy to 72%.[52] This study also used a CNN (DL) but using pre-trained weights and fine-tuning to skin lesion photographs. This extensive study demonstrated that bigger sample sets get more generalized but maybe low accurate results. Nonetheless, comparing the 72% model accuracy with 21 trained dermatologists, the model was still more accurate on average than the physicians, who obtained an accuracy score of 66%.[52]

Despite the higher number of reports in this field, there is a big scientific gap to be filled concerning computer-aided diagnosis and fluorescence lifetime imaging systems, especially when considering clinical instrumentation validation. The reported studies used tissue slide images (*ex vivo*), and animal models, as shown in sections 2.2 and 2.3, and uses mainly benchtop optical devices not feasible to clinical implementation. Therefore, the present study aims to contribute to the field providing big *in situ* fluorescence lifetime image dataset of skin lesions in human patients, and validating the optical instrumentation and analyses using computational methods.

3 THEORETICAL CONCEPTS

3.1 Basic principles of fluorescence

When light reaches a molecule, photons can be scattered or absorbed. In general, the radiation emitted by the first process has the same or almost the same wavelength of the excitation, while the second process has a distinct wavelength. These two main processes are called scattering and luminescence, respectively. At room temperature, most molecules are in their lowest energy state, called ground state. Due to their electronic structures, molecules can absorb photons, which result in an increase of energy, and their transition to excited and less stable quantum states. For this excited molecule to return to the equilibrium state, it has to dissipate the absorbed energy, which can occur by either non-radiative or radiative (luminescent) decay processes. In the first one, energy is released through vibrational relaxation or energy transfer, while in the second one, energy is released through photon emission. Luminescent decay processes are classified into two types, fluorescence, which occurs when the spin multiplicity is not altered between the initial and final states, and phosphorescence, when the spin multiplicity is altered due to the intersystem crossing intersection before the photon emission.[37]

Before explaining luminescence processes, one must assume the Born-Oppenheimer approximation, for which nuclear and electronic displacements and movements can be mathematically separated for one molecule. This involves assuming that electron motion is much higher than nuclear motion. Furthermore, it is also important to consider the Franck-Condon principle, which states that when a molecule undergoes an electronic transition (absorption/emission of photons), the nuclear configuration has no significant change. It is not only due to the fact that the nucleus has much higher mass than electrons, but also because electronic transitions are faster than any change that might occur at the nucleus. In addition, this principle defines that the absorption spectrum consists of several discrete energy levels rather than a single electronic level. This is due to the fact that nuclei when atoms are structured in molecules undergo Coulomb forces influenced by all electrons and nuclei of neighbor atoms. Then, when excited, these coulombic forces are changed, leading to a new alignment of the nucleus that provokes its vibration.[37]

A typical Jablonski diagram is shown in Figure 3.1. It represents an isolated and ideal molecule, and the luminescence phenomena described above will be explained based on it. Singlet ground state (S_0), first singlet excited state (S_1), and triplet excited state (T_1) are

represented by horizontal dark lines, and fluorophores' states can exist at different vibrational energy levels (represented by 0, 1, 2…). Vertical arrows represent transitions between the states and their length and color represents transitions' energy and wavelength.[37, 54]
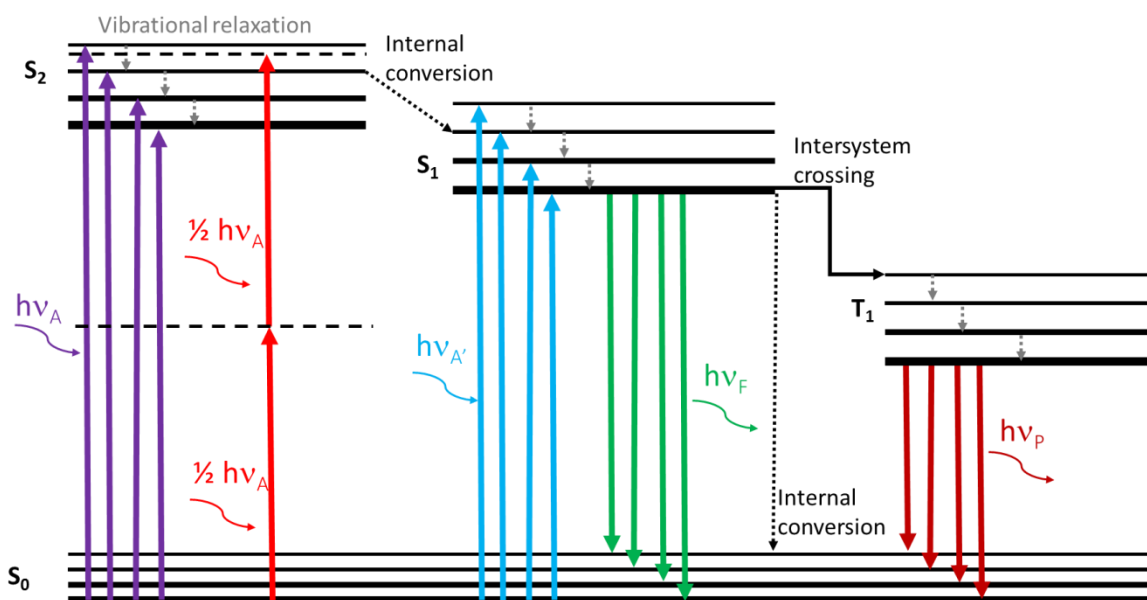
Figure 3.1 - Jablonski Diagram. Firstly, light is absorbed by the system (arrows pointing upwards in violet, blue and red). By vibrational processes (gray arrows) the system can dissipate absorbed energy. It can return to singlet states or to ground state non-radiatively by internal and external conversions (dashed black arrows). Also, the system can change from singlet to triplet states by intersystem crossing (solid black arrow). Finally, it can dissipate energy by emitting a photon by fluorescence or phosphorescence (green and deep red arrows respectively).
Source: By the author.

Transitions for energy absorption typically occur at time intervals of the order of 10^{-15} s (Franck-Condon principle). The excited fluorophore must be at an excited electronic level such as S_2, and to return to the ground state, there is initially an energy loss by non-radiative decays, i.e., the absorbed energy is dissipated by molecular vibrations, collisions, and transfer of energy between molecules (Kasha rule). Non-radiative processes occur over 10^{-12} s.[37] After vibrational relaxation, if the fluorophore still has sufficient energy to migrate to another excited singlet state it does so by internal conversion (S_2 to S_1). In this process, the molecule reaches another state, still excited, but with lower energy and without going through changes of spin multiplicity (singlet-singlet or triplet-triplet). This conversion is quite efficient when the two levels are close in such a way that their vibrational states overlap. It can also occur between S_0 and S_1 however it is less likely.[37]

Ground state return from the lowest vibrational level of excited state can still occur by an allowed transition by an electric dipole, and the selection rules that determine these

transitions are: $\Delta l = \pm 1$, $\Delta m = 0, \pm 1$, and $\Delta s = 0$, with a null total spin variation. Lifetime, i.e., the time during which the molecule stays in this excited state before decaying is of the order of 10^{-9} s, which may vary widely because it depends on the interactions that this molecule is suffering from medium or other molecules. This type of radiative process is called fluorescence. [37, 54] When the electron is in the excited state S_1 it may undergo an intersystem crossing and convert to the first triplet state T_1. In that case, unlike the previous one, there is a non-zero variation in the value of the total fluorophore spin ($\Delta s = 1$). Emissions from this state are prohibited by the dipole selection rules; however, they can occur through interactions of electric quadrupole ($\Delta s = 0$). This radiative decay is called phosphorescence, and the lifetime of these states are much longer, reaching orders of magnitude of 10^{-3} s and longer.[37]

Other modes of molecule photon absorption still exist, one of which is a non-linear process where two low energy photos are simultaneously absorbed to reach a singlet excited state. In those cases, a single low energy photon cannot be absorbed because it has no resonant energy matching the transition level to be achieved, and thus it cannot stimulate radiative decays. However, the excitation energy for such transition level can be achieved if two low-energy photons reach the molecule within a time interval of approximately 10^{-16} s, so that their energy altogether can reach the excitation threshold. This type of light absorption has a rather low probability of occurring at moderate light intensities, so to activate these transitions, high-intensity focused lasers at ultrashort pulse regimes are used, the so called volumetric and time confinement, allowing the two-photon absorption. [37, 55]

The time-independent fluorescence intensity (F_{t-i}) of a set of molecules, also called its steady-state fluorescence, depends on several factors and can be calculated as showed in Equation 1, depending on light intensity of excitation source (ϕ), photon energy ($h \cdot v$) (where h is the Planck constant and v is the electromagnetic wave frequency), fluorescence detection efficiency (E), extinction coefficient (ϵ), fluorescence quantum yield (Ξ), fluorophore concentration (C).[37]

$$F_{t-i} = \frac{\Phi . E . \epsilon . \Xi . C}{h . v} \tag{1}$$

On the other hand, time-dependent fluorescence intensity can also be calculated and it is based on the variation of the number of excited molecules ($n(t)$) at a time (t) after the excitation (Equation 2).[37]

$$\frac{dn(t)}{dt} = (k_r + k_{nr}) \cdot n(t) \tag{2}$$

The emissive rate is k_r, while k_{nr} is the non-radiative decay rate. As an emission is a random event, and each excited fluorophore has a probability of emitting in a given period of time, the solution of this equation results in an exponential decay function for the excited population: $n(t) = A \cdot e^{-t/(k_r + k_{nr})}$.[56] Integrating Equation 2 in the number of excited molecules would give fluorescence intensity ($F(t)$), being dependent on the decay time (also called lifetime) of fluorescence, being the inverse of the total decay rate $\tau = (k_r + k_{nr})^{-1}$. However, as mentioned above, different fluorophores, or even the same fluorophore, can show wide different decay rates due to interactions between molecules or mediums. Hence, decay equation solution can be a combination of N exponential decays as shown by Equation 3. [37, 56]

$$F(t) = \sum_{i=1}^{N} w_i \, e^{-\frac{t}{\tau_i}} \tag{3}$$

Where τ_i is the decay time and w_i is the weight of this exponential, leading to the calculation of average fluorescence lifetime (τ_{avg}) by Equation 4.[37, 56] By integrating Equation 3 in time, it is also possible to calculate the steady-state (time-independent) fluorescence intensity.

$$\tau_{avg} = \frac{\sum_{i=1}^{N} w_i \, \tau_i^2}{\sum_{i=1}^{N} w_i \, \tau_i} \tag{4}$$

When applying this concept, the number (N) of exponential decays can vary widely, depending on the system temporal resolution, and the studied application. Usually, in the biomedical optics field of research, N is set to two and associated with bound and free fraction of the studied molecules.

These principles and equations are valid for any fluorophore. If working with several fluorophores at the same time, the most important parameters to differentiate them are the fluorescence emission range and lifetime. In general, emission range differences are used to differentiate between two distinct fluorophores, whereas lifetime is used to evaluate the molecule micro-environment. These parameters can carry information that allows distinguishing between many molecules at the same time, as well as to know the proportion between bound and free states in the fluorophores, or even the distance range between two molecules (using FRET). Thus, they can be used to take information even from tissues that have many different molecules and environments.

3.2 Endogenous fluorescence

Endogenous fluorescence, autofluorescence, label-free fluorescence, or native fluorescence are given names to a widespread phenomenon of biomolecules acting as fluorophores in many organisms and gained prominence since the 1900's with the technological progress in microscopy and spectrofluorimetry.[21, 57] Main biological fluorophores correspond to proteins, amino acids, and coenzymes, hence biomolecules steady-state and lifetime fluorescence carry information from morpho-functional to metabolic changes in tissue or in single cells.

Two of the main endogenous fluorophores (NADH and FAD) are related to mitochondrial function, acting on the support of the energy demands on cell processes. Since mitochondrial anomalies are widely linked with a range of diseases, including cancer, these fluorophores play a key role in the optical diagnosis. Moreover, it is also known that collagen and elastin native fluorescence is changed depending on the fibroblast's proliferation direction, the arrangement of the fiber, and also on inflammatory processes, that can be features of tumor progression.[58] Table 3.1 summarizes endogenous fluorophores types and major excitation and emission wavelength ranges.

Table 3.1 - Summary of relevant diagnostic features of the main endogenous fluorophores.

Endogenous fluorophore	Biological constituents	Fluorescence ranges (ex nm) / (em nm)
Tryptophan	Amino acid	200 – 220 / 320 – 360
Cytokeratin	Intracellular fibrous proteins	280 – 325 / 495 –525
Collagen/Elastin	Extracellular fibrous proteins	330 – 380 / 360 – 450
NADH	Coenzymes	330 – 380 / 440 – 470
Flavin	Coenzymes	350 –370 / 480 – 540
Fatty acids	Accumulated lipids	330 – 350 / 470 – 480
Vitamin A	Retinols and carotenoids	370 – 380 / 490 – 510
Porphyrin derivatives	Protein prosthetic group	405 / 630 – 700

Source: Adapted from CROCE, BOTTIROLI. [57]

Cancer is known by showing significantly higher metabolic activity and asymmetric growth caused by the altered physiological properties of the tissue. As a result, the endogenous fluorophores show differences in steady-state and lifetime fluorescence properties, carrying the information of the altered tissue. Hence, these biomolecules act as intrinsic optical biomarkers (OB), allowing real-time characterization, monitoring of tissue status, and lesion screening.[21, 57] For these reasons, the OB patterns certainly are great inputs for a diagnostic technique.

3.3 Basic principles of machine learning

Search for patterns in data is a fundamental method not only in scientific research but in all human life perceptions. Repetitive patterns are associated with different phenomena since the beginning of human history. For instance, Tycho Brahe, a Danish astronomer who lived in the 16th century, performed astronomical observations without a telescope and built a detailed dataset of the positions of stars, the moon, and Mars all over the years. These records allowed another scientist, Johannes Kepler, to the discovery of the empirical laws of planetary motion based on the regularities detected in Tycho data, which allowed an extensive field of classical mechanics based on repetitive patterns. Similarly, quantum mechanics theoretical and experimental development and validation were also based on regularities in atomic and molecular spectra. [59-60]

Pattern recognition, machine learning (ML) and artificial intelligence (AI) are common terms to describe a field that is concerned about the automatic discovery of regularities (patterns) in data through computer algorithms. These algorithms use a database (D) composed by vectors or matrices as input $\vec{X} = \{X_1 \dots X_N\}$; each $\vec{X}$ is an observable (sample), while each $\{X_1 \dots X_N\}$ is a feature. The algorithms assume that exists a function $f: \vec{X} \to Y$ that fit the inputs ($\vec{X}$) and respond to the correct output (Y), and, by many fitting methods, tries to model a function $g: \vec{X} \to Y$ automatically. ML algorithms work to optimize the functions to be similar (i.e., to make $g \simeq f$).[59]

ML may have different types of outputs $Y(\vec{X})$, such as continuous numbers in case of regression, e.g., the content of a chemical element in a sample, or classes in case of classification, e.g., diseased or healthy patient. With the higher development in this field of research in the last decade, algorithms became powerful, being able to outperform humans in different tasks, and having multiple outputs. [59-60]

Some ML applications have labeled databases that are known as "supervised learning", which can be divided into regression and classification types, whereas "unsupervised learning" does not require its database to have labeled data. In supervised learning, the database is often split into two types of sets: training and test sets. The training set is used to fit the model and tune the parameters. In the case of a classification task, the ML model has a threshold set in the training set, which allows the algorithm to determine the class assigned to the samples. Finally, the test set is used to ensure that the model fitted in the training set is general enough to fit

another sample set with the same features. [59-60] Figure 3.2 shows a basic setup of supervised ML.
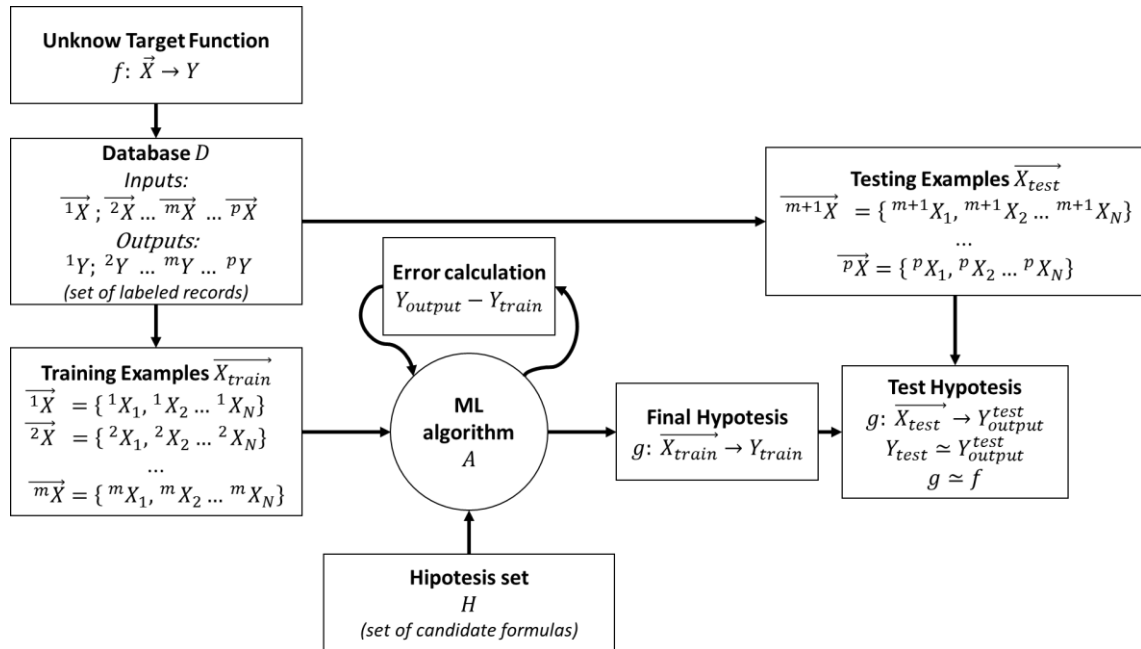
Figure 3.2 - Basic setup of a supervised ML problem.
Source: Adapted from ABU-MOSTAFA.[59]

The central fundamental of the ML field is the probability theory. It allows manipulating the uncertainty which arises both by the noise on the features of the dataset (measurements) and by the finite size of datasets. A key concept of ML is the Bayes theorem, which arises from the sum and product rules on probability theory and is shown in Equation (5).

$$P(A|B) = \frac{P(B|A)P(A)}{P(B)} = \frac{P(B|A)P(A)}{\sum_A P(B|A)P(A)} \qquad (5)$$

Briefly, the Bayes theorem states the probability of an event A given that B event happened ($P(A|B)$), based on the prior knowledge of the probability of B to happen given that A happened ($P(B|A)$) and the entire probabilities that B or A happens (i.e., $P(B)$ and $P(A)$). This rule is the basis of the ML field. It states that if the first observable ($\overrightarrow{^1X}$) on the dataset has a regularity, and the second one ($\overrightarrow{^2X}$) has the same pattern, they can be labeled as part of the same class ($^1Y = {}^2Y$), and the probability for this decision to be made increases with the similarity of the regularities observed, thus increasing the likelihood of a correct classification.

Henceforth, all the other observable in the training set can be compared to each other, so that every time the same regularity appears, the method will label it as part of the same class.[59]

Evaluation of ML models vary in terms of the type and the task (classification or regression) of the model. Metrics can be calculated from the models outputs and are useful to analyze their potential to correctly predict test samples. The most used metric is the overall accuracy, which is calculated by the ratio of the number of correctly classified samples and the number of samples in the entire. Two other similar metrics are important: the sensitivity (also kwon as true positive rate or recall), and the specificity (true negative rate). Sensitivity is calculated as given ta disease condition, how likely the model is to detect it, which means to divide the number of diseases correctly classified by the model by the total number of diseases (true positive rate). On the other hand, specificity is calculated as given a healthy condition, how likely is the model to detect it, which means to divide the number of healthy tissue correctly classified by the model by the total number of healthy diseases.

Sensitivity is a key metric in cancer detection since higher sensitivities means that lower disease tissues were misclassified, even if this rise specificity, which means that some healthy tissues were classified as cancer as well. A common method to set a threshold to the model classification and to compare models is the receiver operating curve (ROC), which plots the sensitivity against 1-specificity and the higher this curve is more its area under curve (AUC) approximates to the value of 1. The ROC AUC and the sensitivity threshold are key metrics to evaluate models to disease detection.

ML powerful models, recently called AI, for healthcare is one of the hottest topics on science in 2020. It is considered a breakthrough in the traditional medical business and the patient and physician relations.[61] It is already present in many types of clinics actuating as diagnostic techniques in many medical areas, such as cardiology psychiatry, endocrinology, radiology, neurology, orthopedics, ophthalmology, and oncology. Until September 2019 the United States (US) food and drug administration (FDA) has already approved 46 AI-based diagnostic techniques. Thus, ML models can notably be powerful and as precise as physicians.[61]

4 OBJECTIVES

The main objective of the present study was the determination of a multispectral fluorescence lifetime imaging model for screening and diagnosis of skin cancer.

4.1 Specific objectives

- Evaluate the characteristic emissions of endogenous fluorophores in normal and cancer cells to identify their individual contributions as optical biomarkers.

- Test different mathematical methods to extract FLIm metabolic optical biomarkers information of the investigated tissues.

- Use the identified metabolic optical biomarker features to distinguish between healthy and abnormal tissues (skin cancer and benign conditions).

- Develop machine learning models for screening and discrimination between different skin conditions.

5   PART A: *IN VITRO* EXPERIMENTS

This section reports a study on the steady-state and lifetime autofluorescence of three different cell types, one normal and two cancer cells, correlating the metabolic rates and the malignant condition. This section demonstrates how the OB features can be used to distinguish between cell types, supporting the motivation for sections 6 and 7 of this study.

5.1 Experimental

5.1.1 Cell culture

Human dermal fibroblasts, neonatal HDFn (PCS-201-010, ATCC), murine melanoma B16-F10 (CRL-6475, ATCC), and human tongue squamous cell carcinoma SCC-25 (CRL-1628, ATCC) cell lines were obtained from Gibco™ and cultured in phenol-red added DMEM (Dulbecco's Modified Eagle Medium – Cultilab®) supplemented with 10% Fetal Bovine Serum (FBS) and maintained in an incubator at 37ºC in humidified atmosphere (95% air, 5% CO_2). All experiments were performed at a cell line passage lower than the 15th. For all microscopy experiments, cells were seeded at a density of $1x10^5$ cells on 3 cm Petri dish and cultured for 24h with DMEM and 10% of FBS. For microscopy imaging, cells were washed twice with PBS solution and the medium was replaced by phenol red-free DMEM medium and 5% of FBS.

5.1.2 Confocal microscopy protocol

Images were acquired by a confocal laser scanning microscope (Zeiss – LSM 780, Zeiss, Jena, Germany). The microscope was operating in two acquisition modes: spectral and channel ones. In the spectral mode, each pixel has a spectrum ranging from 400 to 700 nm with 9 nm resolution, thus, the image is colored using the spectrum of each pixel. Whereas, in channel mode, each pixel has two spectral bands acquired and the image is colored as the user chooses. Ranging from 400 to 500 nm, the first channel acquired the fluorescence signal related to NADH, while for FAD acquisition, the 500 to 600 nm spectral band was set. Two-photon excitation was used in all samples, a Ti:Sa (Chameleon Vision II, Coherent Inc., Santa Clara, Canada) pulsed laser (100 fs) was used at two different wavelengths. For NADH imaging, 755 nm excitation wavelength was used. For FAD imaging, 860 nm was used as excitation wavelength. Images were acquired in 1024 x 1024 pixels with 6.3 µs pixel-dwell time,

magnifications of 20x and 63x, using a heat plaque with the temperature set to 38 ℃. Five images were acquired for each cell type and one for a free NADH solution.

FLIM images were acquired by the same microscope setup, in the same magnifications but in 512x512 pixels. Time correlated single photon counting (TCSPC) single-photon avalanche diodes (SPAD) detector was used in this system to acquire NADH lifetime images (same acquisition band of steady-state fluorescence 400-500 nm).

Five regions were imaged for each cell type, both in the steady-state mode, and the FLIM mode. Moreover, for comparison, one image was performed in each mode for a free NADH synthetic solution.

5.2 Data processing

Confocal microscopy images of NADH and FAD and FLIM NADH images were processed using MatLab R2012 (Mathworks) and Python 3. As native fluorescence has a weak signal, images had a poor signal-to-noise ratio and showed salt and pepper noise (white and black pixels noise). Then, the first step was to exclude the noise by a fast Fourier transform (FFT) Gaussian filter in two dimensions in the frequency domain, followed by a Gaussian smoothing of 3 pixels window in the spatial domain.

For steady-state confocal microscopy images, a binary mask was created by selecting which image (NADH or FAD) had the higher signal-to-noise ratio. In the fibroblasts case, FAD image was chosen, whereas for melanoma and SCC the NADH image demonstrated a higher signal-to-noise ratio. To create the mask, edges of the images were detected, dilated, and then the region inside the edges was filled. The same mask was applied both to NADH and FAD images. As these coenzymes play a key role in cell energy metabolism, it is important to study the relation between then, called Optical Redox Ratio (ORR).[21] To create the ORR images, each pixel of the FAD image was divided by the sum of the pixels of NADH and FAD images (Equation (6)).

$$ORR = \frac{FAD}{NADH + FAD} \tag{6}$$

With the ORR images, histograms of the pixels were performed and the median value of the histogram was taken to allow further comparisons.

For NADH FLIM images, the mask was created using the intensity of each pixel. Then, by the fast FLIM algorithm, the average lifetime for each pixel was calculated based on the centroid of the fluorescence decay. Histograms of the average lifetime were generated to allow comparisons between cells and the free NADH solution. Finally, the average decay curve of the entire image was calculated taken into account each pixel decay, and a bi-exponential decay curve (Equation (7)) was fitted to the fluorescence decay ($f(t)$).

$$f(t) = w_{fast} \cdot e^{-\frac{t}{\tau_{fast}}} + w_{slow} \cdot e^{-\frac{t}{\tau_{slow}}} \tag{7}$$

The bi-exponential decay presents a fast and a slow lifetime (τ), related to the bound and free fraction of NADH, respectively. Since the weights (w) are normalized, they are linearly related, then just the slow lifetime-weight was used in the analysis of this section.

5.3 Results

Typical two-photon excitation image of NADH and FAD fluorescence intensity in cells is shown in Figure 5.1 (A) and (B) respectively. Images of Figure 5.1 were generated on the spectral mode, thus, the blue and green fluorescence colors for NADH and FAD are real colors.
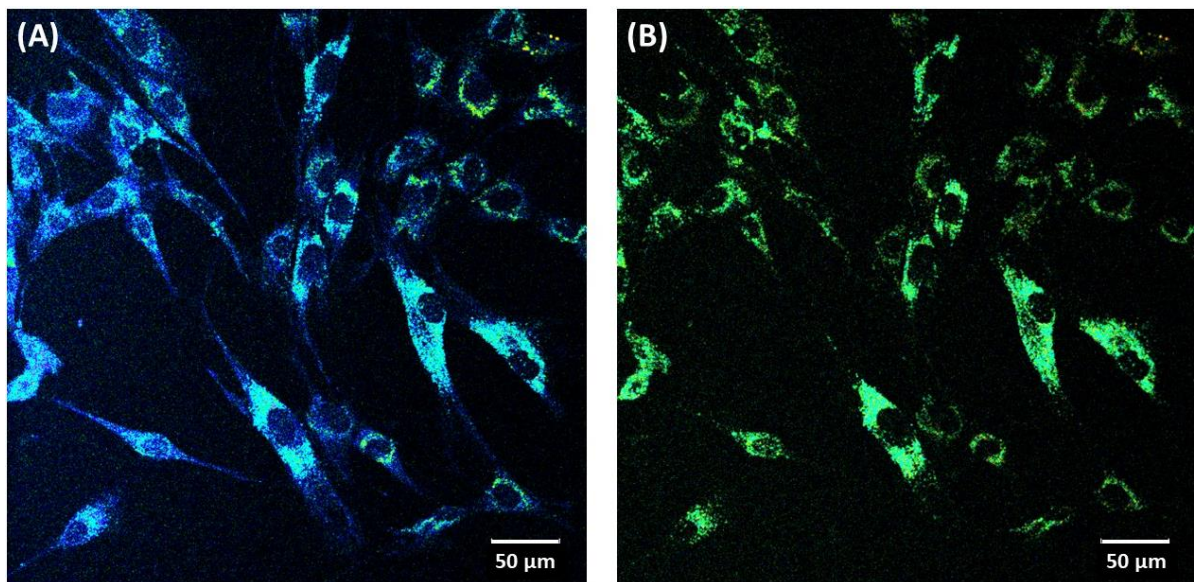
Figure 5.1 - Two-photon spectral microscopy images of fibroblast cells. Autofluorescence of NADH (A) and FAD (B) are represented by the true colors (acquisition range 400- 700 nm).
Source: By the author.

Applying Equation 6 for each pixel of the images from Figure 5.1, the ORR maps for each cell type were generated and the results are shown in the left column of Figure 5.2. Colors represent the ORR for each pixel, from blue to yellow, the maps show lower and higher ORRs'.

Figure 5.2 (A), (C) and (E) shows an example for Fibroblasts, melanoma, and SCC cells, at this point, it is important to remind that the first one is a normal cell, and the last two are distinct cancer cells. For comparison, FLIM images of the same region are shown in the right column of Figure 5.2 (B), (D) and (F) for fibroblasts, melanoma, and SCC, respectively. Each pixel brightness represents NADH fluorescence intensity, whereas the false colors represent the average lifetime fluorescence for each pixel. Blue color represents lower average lifetimes, and the red color represents a higher average lifetime.

Comparing the cell types in the left column of Figure 5.2 it is possible to observe a very distinct ORR value for the three images, showing a higher value for fibroblasts, a medium one for SCC and a lower value for melanoma. This trend is shown in Figure 5.3 (A), where the median value of the histograms of each of the five regions imaged is shown. The green boxplot represents the fibroblasts, whereas the SCC cells are represented in the red boxplot, and the black one is representing melanoma cells. Another ORR feature is that the normal cells showed a more discrete distribution, meaning that they are more homogenous, when compared to the malignant cells.
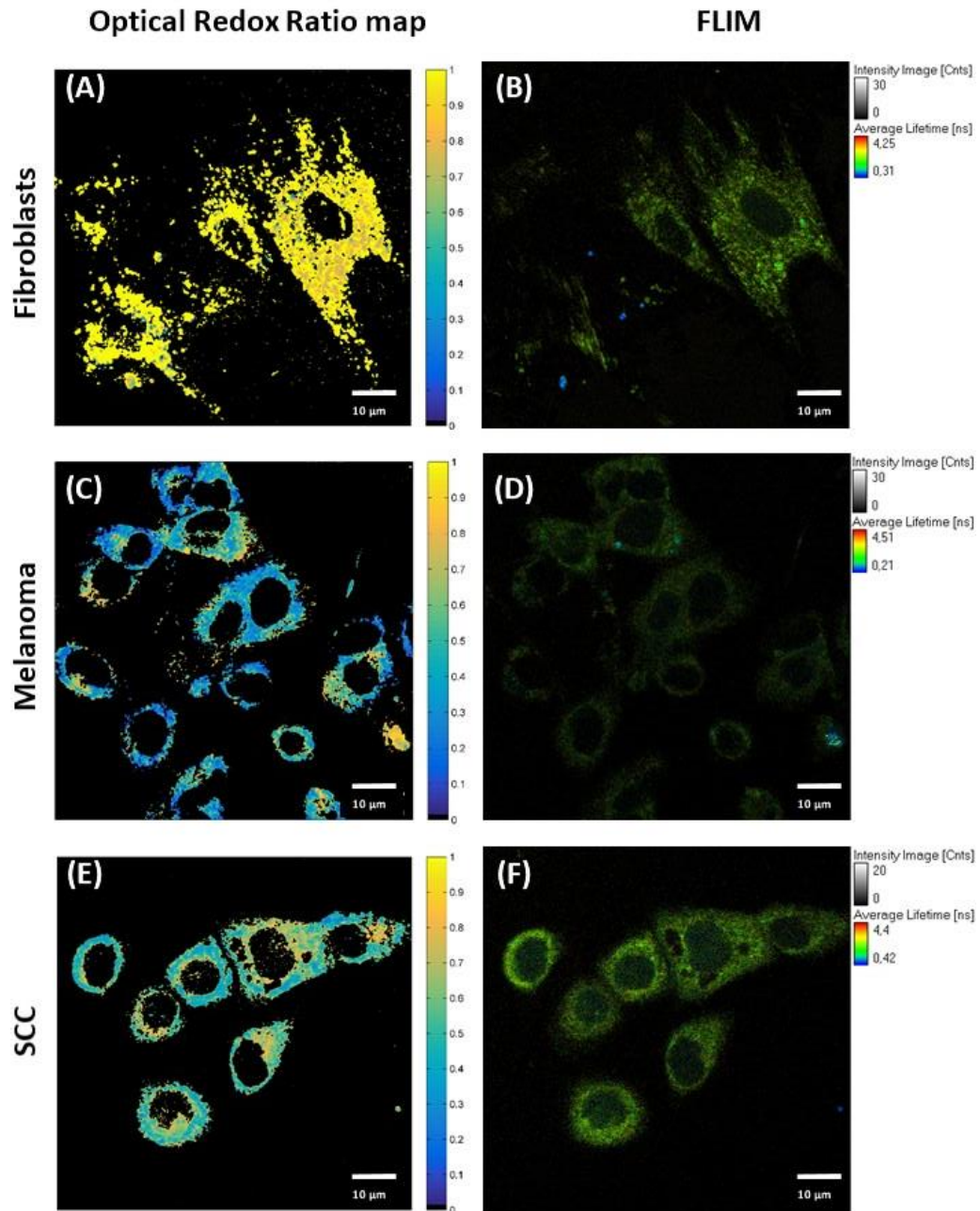
Figure 5.2 - Optical redox ratio map (left column) and FLIM images (right column) of Fibroblasts (A - B), Melanoma (C - D), and SCC cells (E - F). False colors represent the ORR (left column) and average lifetimes (right column).

Source: By the author.

On the other hand, the differences in the FLIM images are not easily observed, since the average lifetime colored images are very similar. However, the histogram of the pixel's average lifetime improves the contrast of the differences between the cell types (Figure 5.3 (B)). The average lifetime shows that fibroblasts cells (green line) have slower lifetimes than SCC cells (red line), whereas melanoma cells (black line) present faster lifetimes, and the free NADH solution presents an even faster lifetime (violet line). By the average decay of the pixels for

each cell type, it was possible to fit a bi-exponential decay (Equation 7) and compare the average fitted lifetime parameters among the three cell types (Table 5.1).
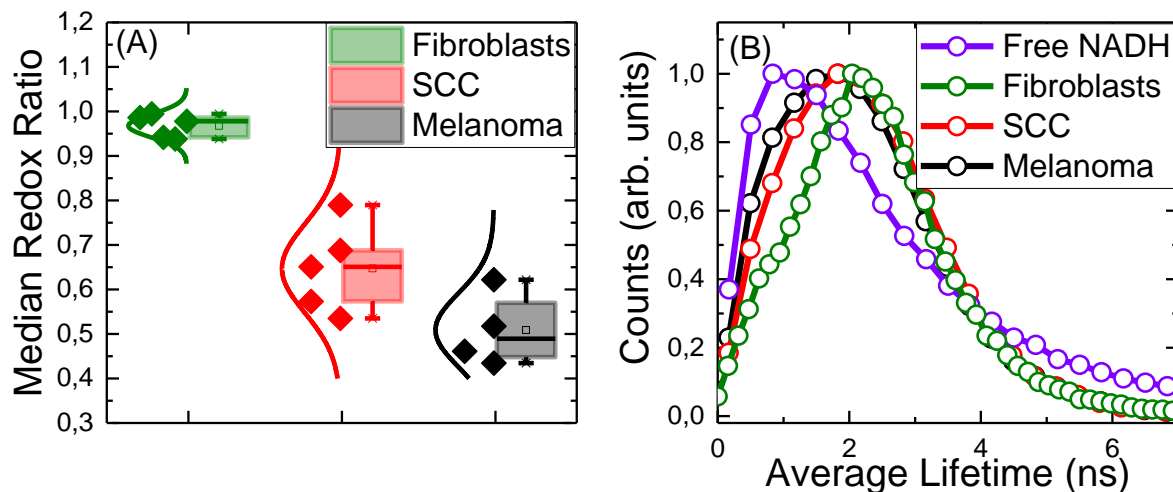
Figure 5.3 - Median optical redox ratio of fibroblasts (green), SCC (red), and melanoma (black) cells (A). Average lifetime histogram of free NADH (violet), fibroblasts (green), melanoma (black) and SCC cells (red) (B).
Source: By the author.

Table 5.1 - Bi-exponential fitted parameter values for each cell line.

	τ_{fast} (ps)	τ_{slow} (ps)	w_{slow} (%)	τ_{avg} (ps)
Fibroblasts	625	2983	30	2208
SCC	608	2984	32	2261
Melanoma	560	2964	22	1996

Source: By the author.

5.4 Discussions

Studying NADH and FAD steady-state and lifetime fluorescence in cells are important to understand not only the contribution of each fluorophore but also to suggest characteristics that should be evaluated for in a clinical study of label-free fluorescence analysis. In this section, the differences of the ORR, the average lifetime, and the lifetime parameters of one healthy cell and two types of cancer cells were demonstrated.

It is well known that mitochondrial anomalies are highly associated with cancer disease. Cancer cells exhibit an elevated level of intracellular NADH and reduced level of FAD, and also have higher intracellular variability.[62-64] Figure 5.3 (A) demonstrated that the ORR of healthy cells is higher than the cancer cells, the higher the ORR, the more oxidative phosphorylation metabolic pathway the cell uses, the lower ORR the more glycolysis is used to produce cellular energy. Fibroblasts showed ORR median around 0.95, whereas SCC and

melanoma cells showed median ORR around 0.65 and 0.48, respectively. This trend between healthy and cancer cells was expected and confirmed in this study, proving that the ORR can be a good feature to distinguish between cancer and healthy tissues.[21, 23, 64]

The higher ORR for SCC compared to melanoma ORRs' can be also due to the higher metabolic rates of melanoma compared to SCC. In an animal model, Skala *et al.*[62] demonstrated that high-grade precancerous tissue had higher metabolic rates compared to low-grade. Concluding that the high-grade shifts from oxidative phosphorylation to glycolysis faster than the low-grade tissue, whereas the healthy tissue showed lower metabolic rate. The results obtained in the present study can be explained by the Warburg effect.[65-66] It describes the energy production by high glycolysis rates in cancer cells, even when the oxygen amount is abundant enough that would favor the oxidative phosphorylation in normal cells. Explaining the reduction of the ORR on cancer cells, even when the oxygen condition is equal for normal cells, which is shown in the present study.

Moreover, it is also known that the intracellular variability is significantly greater in the cancer cells compared to the healthy cells, leading to longer boxplots in Figure 5.3 (A). In different cells and conditions, mitochondria are localized in different regions and may have distinct morphology, biochemical properties, and interact with other intracellular structures.[63]

The heterogeneous mitochondrial function and micro-environments also lead to different fluorescence NADH lifetimes (Figure 5.3 (B)). This study demonstrated that NADH average lifetimes are lower for melanoma and SCC compared to the fibroblasts cells, which corroborate with *in vitro* [23, 67] and *in vivo* [23, 68] studies.

Literature reports show that not only the average fluorescence lifetime but also the fast and slow (free and protein-bound) NADH lifetimes decreased when the cells were put in an environment with a lack of oxygen. This is observed because this condition favored glycolysis on cells, which is the same pathway that cancer cells favor to energy production. [23-24, 62-63, 69] Thus, it is possible to infer that the lifetimes are also varying with the metabolic rate, as shown in Figure 5.3 (B) and Table 5.1.

Despite the average lifetime histograms clearly show this trend, the calculated τ_{avg} shown in Table 5.1 is very similar among all cell types. In particular, SCC average lifetime is longer than fibroblasts cells, which is not clearly shown in the histogram. Given these points, the importance of the other parameters of the bi-exponential fitting is emphasized since they can be very different among the cell types. In this context, the lifetime parameters are key features to obtain the real protein-bound and free states of NADH in the cells, and for these

reasons, they may increase the potential of discrimination of malignant and benign tissues in clinical studies.

5.5 Final remarks

In conclusion, this section demonstrates how the intrinsic metabolic activities of the cells are correlated and can be measured by the steady-state and lifetime autofluorescence. Cancer cells demonstrated lower values for ORR when compared to normal epithelium cells, indicating mitochondrial dysfunctions that shift energy metabolism from oxidative phosphorylation to glycolysis. Additionally, due to the metabolism rate, even the cancer cells demonstrate differences in the ORR values, being lower for melanoma than SCC.

As well as ORR, lifetime parameters also showed to be important biomarkers to the cell metabolic activities. Despite lifetime histograms for cancer cells showed to be very distinct from healthy cells, the average lifetime (τ_{avg}) calculated by the decay curve fitting does not show great differences among the cells. As a result, the fast and slow lifetimes (τ_{fast} τ_{slow}), as well as the lifetime weight (w_{slow}) parameters showed higher differences among the cell types, indicating micro-environment differences for protein-bound and free molecules, also related to the cells' metabolic rate.

Together, the intracellular co-enzymes (NADH and FAD) fluorescence signals are powerful natural biomarkers for mitochondrial anomalies. The ORR and lifetime parameters can be used to track metabolic changes in clinical studies.

6   PART B: FLIm DERMOSCOPE TO DISTINGUISH nBCC AND HEALTHY SKIN

This section reports on a time-domain FLIm dermoscope and demonstrates its capability to clinically perform multispectral fluorescence lifetime dermoscopy of nodular BCC (nBCC) lesions, differentiating it from the surrounding tissue. Further, a comparison between the use of steady-state and lifetime parameters for screening and classification is performed in order to infer the improvement potential based on FLIm data. In this first part of the clinical study, the FLIm dermoscope was validated for clinical use and diagnostic resolution was evaluated through the data analysis of a subset of skin cancer. The results of this section were published at the Photodiagnosis and Photodynamic Therapy journal on the beginning of 2020.[70]

6.1 Experimental

6.1.1 FLIm system

The FLIm dermoscope used in this study was adapted from a previous design [48] and assembled during a previous work.[71] Briefly, the FLIm dermoscope operates on time-domain by measuring the fluorescence decays with a fast detector and digitizer. Figure 6.1 shows the portable FLIm setup. Light from a Q-switched pulsed Nd:YAG laser (<2 ns pulses) emitting at 355 nm passes through a beam splitter (BS) before being coupled by a lens (L1) to the 4 m-long excitation fiber (50 µm core diameter). The split beam (10%) then reaches a detector to trigger the acquisition digitizer. From excitation fiber, the laser beam is delivered to the handheld probe and after passing through a collimation lens (L6), it is redirected by a dichroic mirror (DM1) to the laser scanning system. Two galvanometric mirrors (GMx and GMy) perform the scanning in horizontal and vertical directions, and before reaching the tissue, the light passes through a relay scan lens system (L3; L4; L5), which is also responsible by collecting the fluorescence and descanning light.

By coupling descanned light with L2 to the 4 m-long collection fiber (200 µm core diameter), tissue fluorescence exits from the handheld probe to go to the spectral splitting system after decoupling by L7. Fluorescence beam is divided into three channels by dichroic mirrors (DM2; DM3) and filters (F1 – 390 ± 20 nm; F2 – 452 ± 22 nm; F3 > 496 nm), each one being coupled by lenses (L8; L9; L10) to fibers of different lengths (S1; S2; S3) of 1 m, 13 m and 25 m.

All the three fibers guide light to a broadband amplifier and then to the same MCP-PMT (Microchannel plate – Photo Multiplier Tube) in different times where the signal is recorded in sequence at 2.5 Gs/s (Giga sampling per second), allowing resolution of 0.4 ns. Control and acquisition are performed by a LabVIEW code in a computer, being able to acquire images in 2.5 s (140 x 140 pixels).
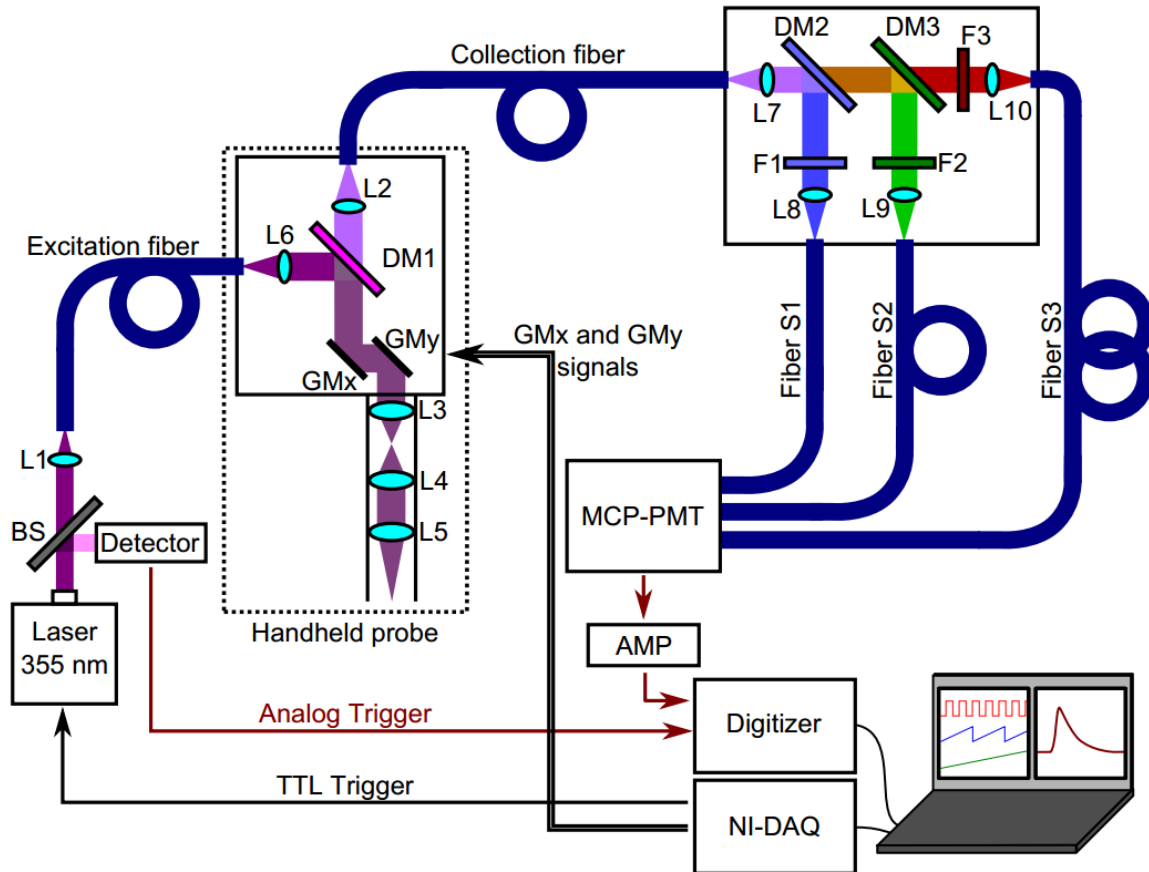
Figure 6.1 - FLIm dermoscope setup: a computer is used to both create the waveforms as well as control and acquire data. Excitation is performed by a Q-switched pulsed Nd:YAG laser (355 nm). A beam sampler is used to split approximately 10% of the beam to the photodetector to trigger the digitizer. The laser is coupled into the excitation fiber and guided to the handheld probe, where it passes the galvanometric scanning system and is guided to the tissue. Backpropagated light is guided by the collection fiber to the multispectral module, and after splitting the wavelength ranges, the signal arrives at the PMT and is acquired.

Source: Adapted from ROSA.[71]

FLIm system was assembled on a mobile cart to provide a suitable clinical use. Figure 6.2 shows pictures of the system mobile cart (Figure 6.2 (A)) at a clinical setting, handheld probe (Figure 6.2 (B)), an example of measurement (Figure 6.2 (C)), and the relation between the lesion and the probe field of view (FOV) (Figure 6.2 (D)).
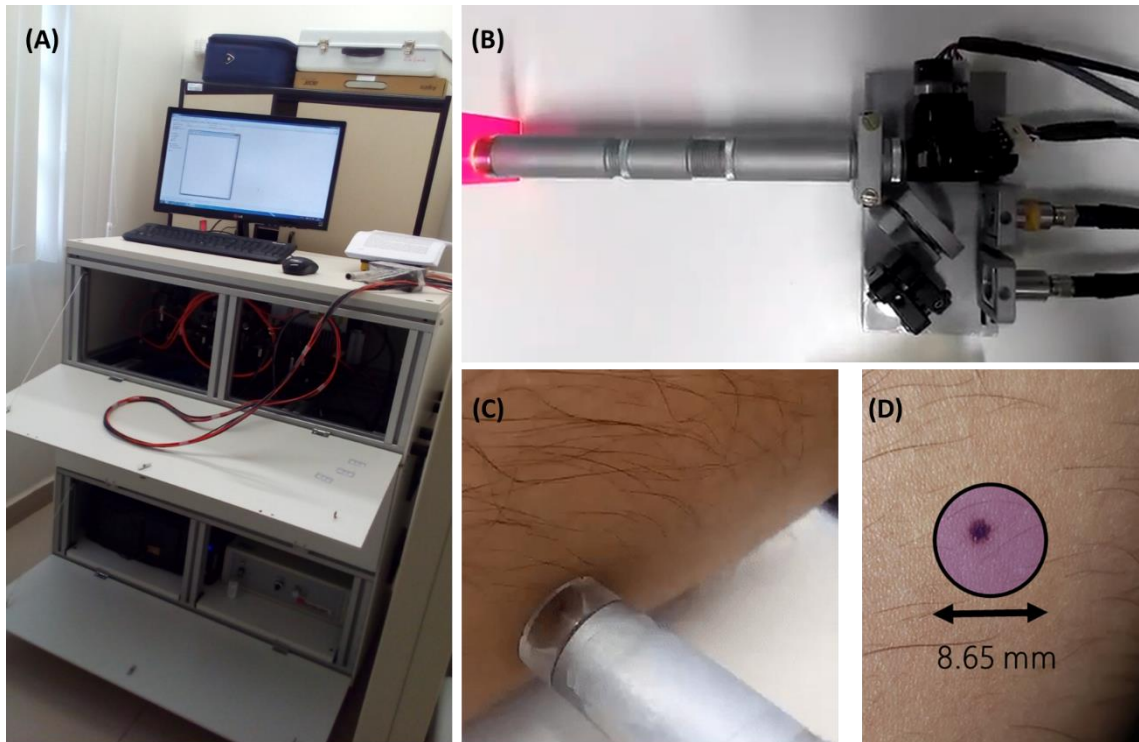
Figure 6.2 - Picture of the FLIm system mobile cart (A), handheld probe (B), an example of measurement (C), and the relation between the lesion and the probe FOV (D).
Source: By the author.

Each channel filter of acquisition and laser of excitation was chosen based on the fluorophore characteristics stated in section 3.2. Figure 6.3 shows the absorption and emission spectra of the main tissue endogenous fluorophores, as well as the laser excitation wavelength and channels of acquisition spectral regions. Consequently, optical biomarkers related to channels 1, 2 and 3 are collagen/elastin, NADH and FAD respectively. Here, it is important to point out that, even though these biomolecules were the main target ones when the acquisition spectral regions where chosen, since the emission signal was originated in a tissue, not in cells or isolated biomolecules, the detected fluorescence is a composition of several endogenous fluorophores and is also influenced by the tissue scattering and absorption.
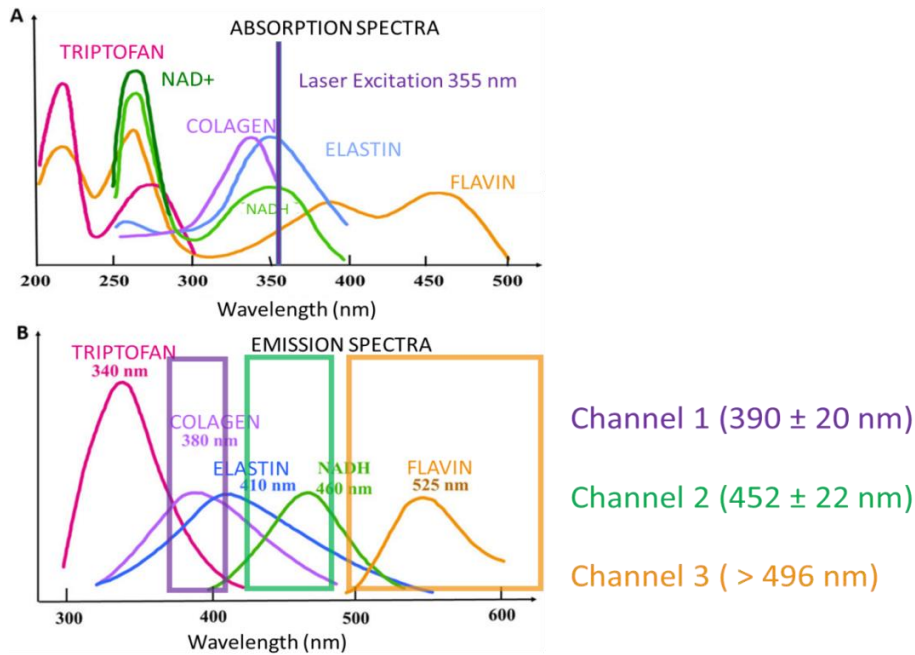
Figure 6.3 - Absorption (A) and emission (B) spectra of the main endogenous fluorophores. Laser excitation is shown as a purple line on (A), and FLIm acquisition channels are shown on (B). False colors represent the main fluorophore spectral emissions.
Source: Adapted from SHI *et al.*[22].

6.1.2 System stability tests

To ensure that the system measurements present the same values over all the experiment, Chroma® standard slides were used to determine portable FLIm stability. Fluorescence standards were measured using an Ocean Optics USB 2000 spectrometer acquiring spectrum from 380 to 750 nm at 3 ms exposure time. Samples were excited using a 378 nm continuous wave laser with 6 mW/cm² of irradiance.

6.1.3 Clinical study

FLIm dermoscope was used to image skin lesions from 38 patients recruited at the Skin Department of the Amaral Carvalho Cancer Hospital (Jahu, São Paulo, Brazil), following an imaging study approved by the Internal Review Board of that institution (CAAE: 71208817.5.00005434). Only patients presenting at least one lesion highly suspected for nBCC and scheduled for biopsy examination were recruited, pigmented and ulcerated lesions were excluded. After signing the written informed consent form, each patient underwent the following imaging protocol right before the scheduled biopsy examination procedure.

First, the suspected nBCC lesion was gently cleaned with a gauze soaked in a saline solution. Then, the tip of the FLIm imaging probe, previously disinfected using a gauze soaked

in ethanol 70%, was placed in contact with the lesion and a FLIm image was acquired. The imaging site was selected so that regions of both lesion and surrounding healthy skin tissues were present within the FOV of the FLIm probe (Figure 6.2 (D)). Right after FLIm imaging, lesion tissue biopsy was performed following standard procedures.

All lesion FLIm images were acquired with an average laser excitation power of 10 mW measured at the sample, a pixel rate of 10 kHz, and 140x140 pixels per image. These parameters corresponded to an acquisition time of 1.96 s and an excitation energy exposure of 1.52 mJ at the sample. For approval by the ethics committee, the usage safety of this equipment was evaluated by a specialized committee taking into consideration specialized scientific literature of similar systems for *in vivo* and clinical applications. [41, 45, 48, 72] The corresponding thermal and photochemical maximum permissible exposure (MPE) levels for skin was calculated, and the present system is in accordance with the guidelines for the American National Standards Institute (ANSI) for Safe Use of Lasers. [73]

6.2 Data processing

The FLIm dermoscope data $y_\lambda(x, y, t)$ is composed of fluorescence intensity temporal decay (t) signals, measured at each emission spectral band (λ) and each spatial location or image pixel (x, y). This data structure is present in each pixel as a vector, which is also called the temporal vector.

6.2.1 Temporal vector corrections

Since some electronic signals have very low-frequency noise, acquired temporal vectors were first corrected by their baseline. Using the first and last 5 points of each one of the three channels, a line was fitted (Figure 6.4 (A)), and, by subtracting this line of the raw data, the baseline of the entire temporal vector the data was corrected.

Further corrections were also performed to avoid bias from the filters and fibers. First, each filter percentage of transmission was measured by a UV-Vis spectrophotometer (Cary Agilent), then each channel was multiplied by the factor of transmission. Since system filters transmissions were on average 70%, 90%, and 50%, the first channel was multiplied by 1.3 factor, whereas second and third channels were multiplied by 1.1% and 1.5% respectively. Second, fiber light intensity loss was estimated by measuring the system instrument response function (IRF) by acquiring the signal of measuring a mirror. Multiplier factors were based on

the decrease of the intensity of the measured light with each one of the fibers of different lengths. The multiplier factors were of 1, 1.12 and 1.17 for first, second, and third channels, respectively. Corrected time vector is shown in Figure 6.4 (B).
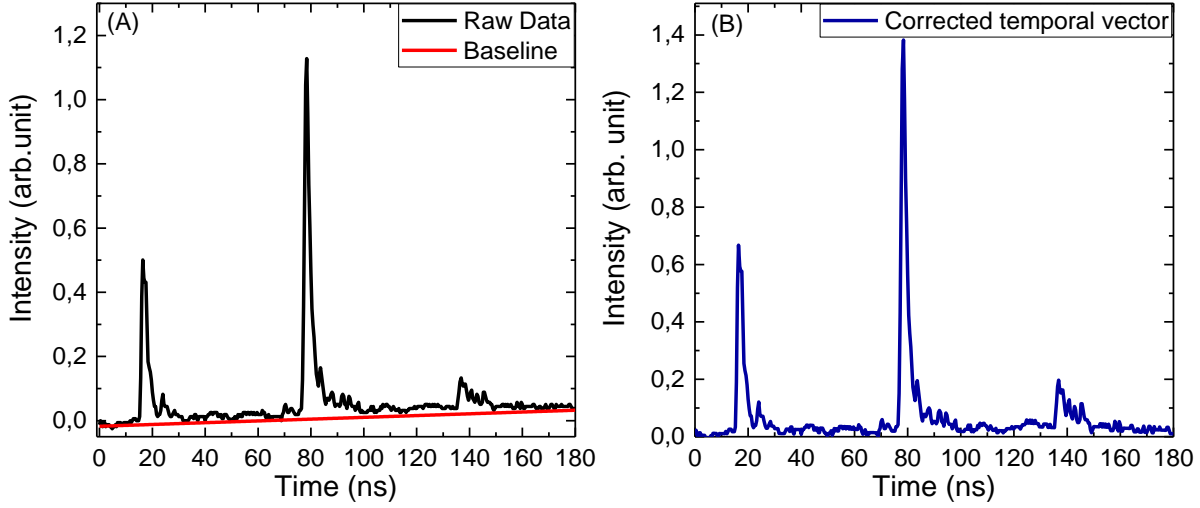
Figure 6.4 -   Raw temporal vector (black line), baseline (red line) and corrected temporal vector (blue line)
Source: By the author.

6.2.2 Optical biomarker feature calculations

With the corrected temporal vector, FLIm dermoscope data is now ready to be interpreted as physical data. The three channels were split at 0-65 ns, 65-130 ns and 130-180 ns respectively.The optical biomarkers features were calculated for each one of the three OB collagen/elastin, NADH and FAD. First, multispectral absolute and normalized fluorescence intensity values were computed for each pixel as follows. The multispectral absolute fluorescence intensity $I_\lambda(x,y)$ was simply computed by numerically integrating the fluorescence intensity temporal decay $(y_\lambda(x,y,t))$ signal:

$$I_\lambda(x,y) = \int y_\lambda(x,y,t)dt \tag{8}$$

The multispectral normalized fluorescence intensity $I_{\lambda,n}(x,y)$ was computed from the multispectral absolute fluorescence intensities $I_\lambda(x,y)$ as follows:

$$I_{\lambda,n}(x,y) = \frac{I_\lambda(x,y)}{\sum_\lambda I_\lambda(x,y)} \tag{9}$$

In the context of time-domain FLIm data analysis, the fluorescence decay $y_\lambda(x, y, t)$ measured at each spatial location (x, y) can be modeled as the convolution of the fluorescence impulse response (FIR) $h_\lambda(x, y, t)$ of the sample and the measured instrument response function (IRF) $u_\lambda(t)$:

$$y_\lambda(x, y, t) = u_\lambda \otimes h_\lambda(x, y, t) \tag{10}$$

Therefore, to estimate the sample FIR $h_\lambda(x, y, t)$, the IRF $u_\lambda(t)$ needs to be temporally deconvolved from the measured fluorescence decay $y_\lambda(x, y, t)$. In this study, temporal deconvolution was performed using a non-linear least-squares iterative reconvolution algorithm, in which the FIR was modeled as a bi-exponential decay:

$$
\begin{aligned}
h_\lambda(x, y, t) = w_{fast,\lambda}(x, y)e^{-\frac{t}{\tau_{fast,\lambda}(x,y)}} \\
+ w_{slow,\lambda}(x, y)e^{-\frac{t}{\tau_{slow,\lambda}(x,y)}}
\end{aligned}
\tag{11}
$$

Here, $\tau_{fast,\lambda}(x, y)$ and $\tau_{slow,\lambda}(x, y)$ represents the time-constant (lifetime) of the fast and slow decay components, respectively; whereas $w_{fast,\lambda}(x, y)$ and $w_{slow,\lambda}(x, y)$ represent the relative contribution of the fast and slow decay components, respectively.

Equation 11 is the core concept of sections 6 and 7. The average fluorescence lifetime $\tau_{avg,\lambda}(x, y)$ for each pixel and emission spectral band were estimated from the FIR $h_\lambda(x, y, t)$ as follows:

$$\tau_{avg,\lambda} = \frac{\int t h_\lambda(x, y, t)dt}{\int h_\lambda(x, y, t)dt} \tag{12}$$

Finally, the FLIm extracted OB are composed of two sets: steady-state and lifetime (dynamic) fluorescence. Using this approach, eighteen properties were extracted from each pixel, reducing image dimensions from 140x140x451 to 140x140x18 (horizontal pixel x vertical pixel x properties) OB.

The first six OB were related to the steady-state fluorescence intensity integrated (I_λ) and normalized ($I_{n,\lambda}$) of each channel. Henceforth, the next twelve OB are related to fluorescence dynamics. Since $w_{fast,\lambda}(x, y)$ and $w_{slow,\lambda}(x, y)$ are weights to each exponential decay (shorter and longer), their sum is constant. In this context, they are linearly related, and then it is not necessary to use both. Based on *in vitro* studies, it is possible to estimate FRET

efficiency by measuring the weight of the slower lifetime component, then $w_{slow,\lambda}(x,y)$ was chosen to be used for each channel as the next three OB (one for each channel).[23, 37-38]

Shorter ($\tau_{fast,\lambda}$), longer ($\tau_{slow,\lambda}$) and average($\tau_{avg,\lambda}$) lifetimes for each one of three channels are the last six OB. Likewise, they were based on *in vitro* studies and they can indicate the bound or free fraction ratios of the studied molecule[23, 38, 74-75] The summary of the extracted OB set is shown in Table 6.1.

Table 6.1 - Summary of extracted optical biomarkers set.

	Steady-State Fluorescence		Dynamic Fluorescence			
	Integrated intensity	Normalized intensity	Slow lifetime weights	Fast Lifetime	Slow Lifetime	Average Lifetime
Channel 1	I_1	$I_{n,1}$	$w_{slow,1}$	$\tau_{fast,1}$	$\tau_{slow,1}$	$\tau_{avg,1}$
Channel 2	I_2	$I_{n,2}$	$w_{slow,2}$	$\tau_{fast,2}$	$\tau_{slow,2}$	$\tau_{avg,2}$
Channel 3	I_3	$I_{n,3}$	$w_{slow,3}$	$\tau_{fast,3}$	$\tau_{slow,3}$	$\tau_{avg,3}$

Source: By the author.

6.2.3 Region of interest selection

FLIm dermoscope images are composed of both regions of healthy and lesion tissue. Then, regions of interest (ROI) in the images were manually selected based on the clinical evaluation of the dermatologist, as well as FLIm feature maps. For each FLIm image, two ROIs were selected: nBCC and healthy. As ROIs had different sizes for each image, the histogram was normalized.

6.2.4 Statistical Analysis

For each ROI, the median value of each feature was calculated. Thus, each imaged lesion provided paired values of each FLIm parameter, corresponding to healthy and nBCC tissue regions from the same patient.

A paired t-test was applied to paired data of each FLIm feature to assess a significant difference in the median value of each FLIm parameter between healthy and nBCC tissue (sample size of 38). The significance level was set to 5% for all paired t-tests, expecting medium and large effect sizes, the test power can be higher than 0.9.

In order to quantify the potential of the FLIm features to discriminate nBCC from healthy tissue, a linear discriminant analysis was performed on three feature sets. The first set

used only the intensity parameters, whereas the second one was built using only the lifetime parameters, and the third classifier was built using both intensity and lifetime parameters. The total set of 76 samples (38 from each class) was split into training and testing sets (75% and 25% of the total respectively). To evaluate the classifiers, the Receiver Operator Curve (ROC) Area Under the Curve (AUC) for the testing set was calculated. The optimal threshold was calculated based on the diagnostic odds ratio.[76]

6.3 Results

6.3.1 FLIm dermoscope system stability measurements

Chroma® fluorescence slide standards spectra were measured under a 375 nm excitation wavelength (Figure 6.5 (A)). Although this wavelength is not the same used in the FLIm system (355 nm) it is still possible to evaluate the fluorescence since it is not far from each other. Furthermore, the main goal of this characterization was to observe the portable FLIm channels working conditions. The average decay vector acquired by the FLIm system is shown in Figure 6.5 (B).
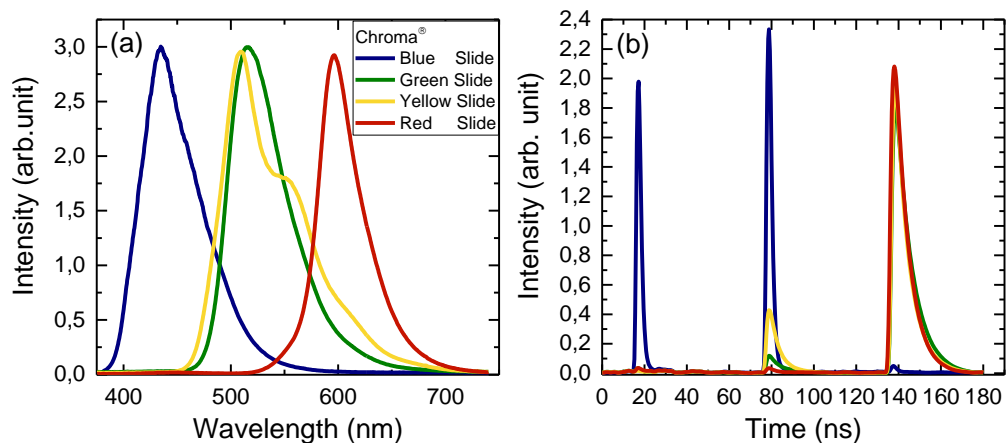
Figure 6.5 - Fluorescence spectra of Chroma® slide standards at 375 nm excitation (a); time vector acquired by portable FLIm system (b). Colors represent the color of the slide.
Source: By the author.

Measurements of the standards were taken in four different days with 90 days of interval One slide was used as the standard for calibrating each acquisition channel: Channel 1 (390 ± 20 nm) was calibrated by the Blue slide, Channel 2 (452 ± 22nm) by the Yellow slide, whereas the Red slide calibrated Channel 3 (> 496 nm). An image of each slide was performed with the same system configuration and pixel average lifetime was calculated for each image on a

different day (Figure 6.6), where colors indicate the corresponding slide. Furthermore, measurements of the same slide (Blue) with different PMT voltages for the acquisition was taken to observe if this would lead to a different lifetime calculation.
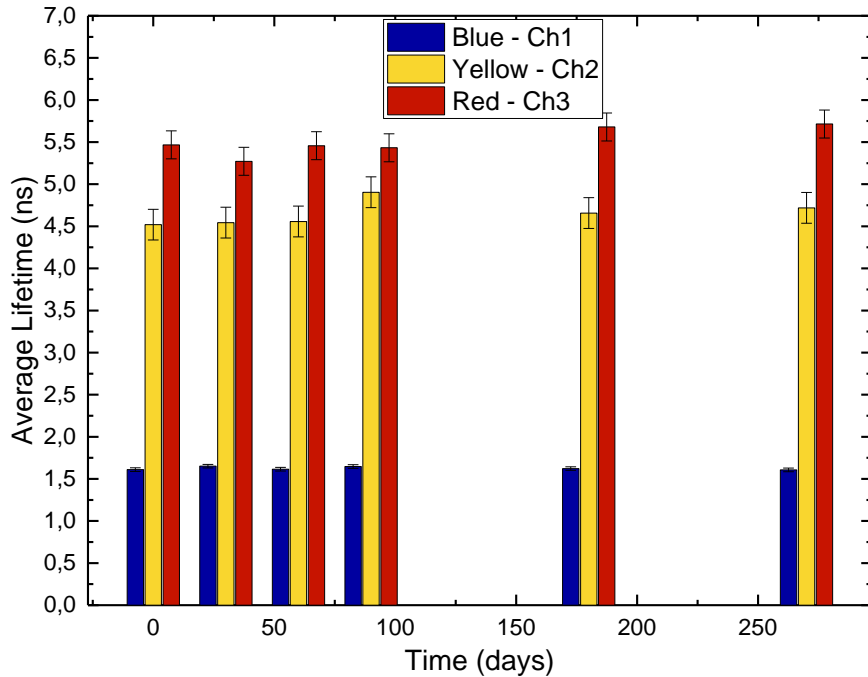
Figure 6.6 - Stability of lifetime measurements of Chroma® slides during days measured with the FLIm system. Source: By the author.

There were no significant changes in the average lifetime for the Chroma® slide during the different days (Figure 6.6). Additionally, it was not observed any significant changes in the average lifetime by performing measurements with different PMT voltage (Table 6.2). These are the expected results, and it is important to note that the system measurements are reproducible.

Table 6.2 - Stability of lifetime measurements of Chroma® slides under different PMT voltages of gain on the FLIm system.

PMT Voltage (kV)	All measurements Average Lifetime (ns)
1.84	1.62 ± 0.02
1.88	1.61 ± 0.02
1.92	1.63 ± 0.03

Source: By the author.

6.3.2 Clinical FLIm Imaging of nBCC skin lesions

A total of thirty-eight (38) skin lesions, confirmed to be nBCC by tissue biopsy

histopathological evaluation, were successfully imaged using the FLIm dermoscope (The system is shown in Figure 6.7 (A)). The clinical digital photograph of a sample skin lesion and its corresponding FLIm feature maps are shown in Figure 6.7 (B) and (C) respectively. This sample lesion corresponds to a nBCC localized on the left arm dorsal region of an 82-year-old female patient, measuring $5x5\ mm^2$ on the surface.

The lesion center region showed lower absolute intensities relative to the surrounding uninvolved tissue (Figure 6.7 – C (i-iii)). Although less contrast was observed between the lesion and surrounding tissue in the relative intensity maps (Figure 6.7 - C (iv-vi)) the lesion region showed increased spatial intensity variability (texture). The lesion center region showed longer average and slow-lifetimes relative to the surrounding tissue in the > 496 nm channel (Figure 6.7 – C (ix, xii)) and shorter fast-lifetimes in both the 390 ± 20 nm and 452 ± 22 nm channels (Figure 6.7 - C(xiii, xiv)). Lower slow-lifetime weight values were also observed in the lesion center region compared to the surrounding uninvolved tissue (Figure 6.7 - C (xvi-xviii)). Overall, these trends in FLIm features observed in this particular lesion are similar with the results (of all samples) from the statistical analysis performed on the ROI mean values, as shown in the next section.

68
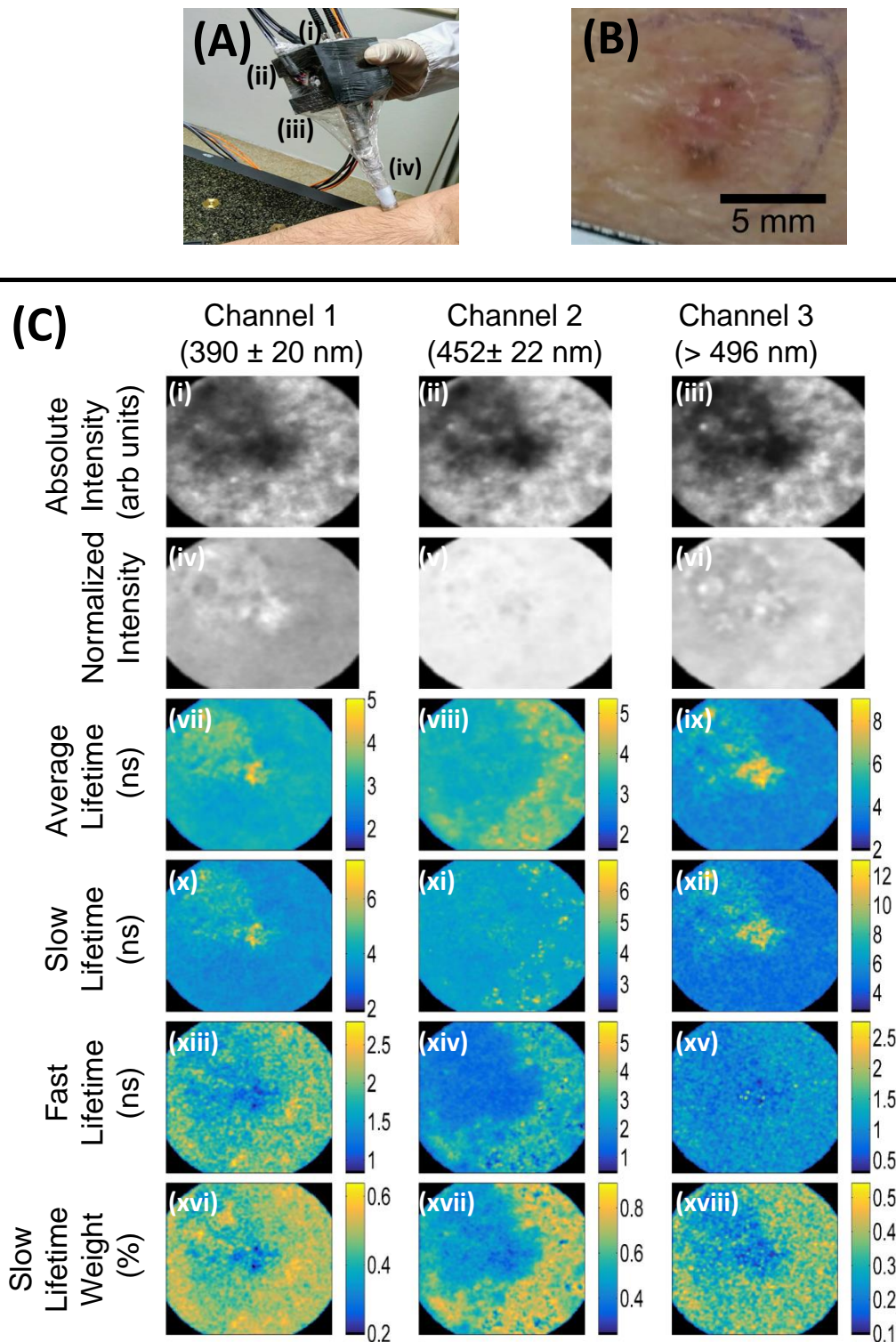
Figure 6.7 - (A) Handheld FLIm dermoscope placed in the forearm region of a human subject. Excitation and acquisition fibers are held in the back of the probe (i); the galvo mirrors controls are held laterally (ii) at the probe printed case (iii); (iv) shows the rigid tube lens. (B) Clinical photography of the imaged nBCC lesion. (C) Multispectral FLIm parameter maps of the nBCC lesion. Columns show fluorescence parameters related to the three detection channels. Integrated Intensity images are shown in the first row; the second row shows normalized intensity images; the third row shows the average lifetime τ_{avg} image; further rows show bi-exponential fitting parameters for the decay: slow and fast decays τ_{slow} and τ_{fast} in ns, and weight w_{slow}. Color maps indicate the values of the weights and decay time, FLIm images are of $8.65 \times 8.65\ mm^2$.

Source: By the author.

6.3.3 Exploratory statistical analysis on FLIm features

A paired t-test was applied to each FLIm feature paired data (n=38) to assess the difference in their ROI-mean values between nBCC and healthy tissue (Figure 6.8). The absolute intensity ROI-mean values for nBCC were significantly lower across all spectral channels ($p < 0.001$, Figure 6.8 (A-C)). For the normalized intensity, the ROI-mean values for nBCC were significantly higher in channel-1 and lower in channel-2 ($p < 0.05$, Figure 6.8 (D-E)). The average lifetime ROI-mean values for nBCC were significantly longer in channel-3 ($p < 0.001$, Figure 6.8 (I)). The slow-lifetime ROI-mean values for nBCC were significantly longer in channel-1 ($p < 0.05$, Figure 6.8 (J)) and channel-3 ($p < 0.001$, Figure 6.8 (L)). In contrast, the fast-lifetime ROI-mean values for nBCC were significantly shorter across all channels ($p < 0.001$, Figure 6.8 (M-O)), and the same trend was observed for the slow-lifetime weight ($p < 0.001$, Figure 6.8 (P-R)).
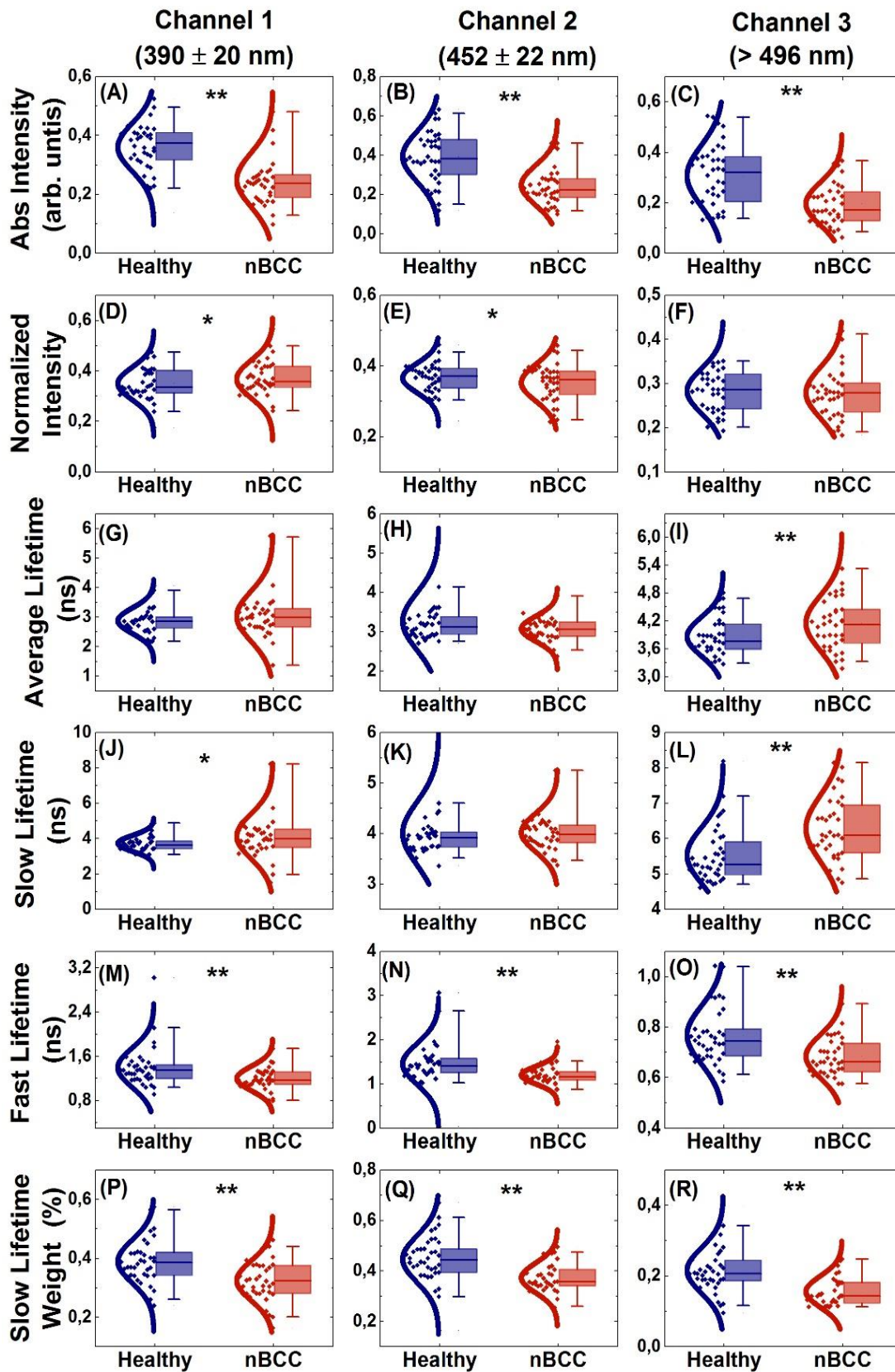
Figure 6.8 -   Boxplots of OB histogram median values for healthy (blue) and nBCC (red) regions. From top to bottom each row represents integrated intensity (arb. units), normalized intensity, average, slow and fast lifetime values (ns), and slower lifetime weight (%). Columns show the three detection channels. Significant differences are indicated by * for P<0.05 and ** for P<0.001.

Source: By the author.

6.3.4 ROC curve analysis

Figure 6.9 shows the test set ROC curves and their AUC for the three classifiers. Features extracted only from lifetime parameters are represented by a solid line and circle markers, whereas intensity only features are represented by a solid line and triangle markers. Gray dashed lines with squares as markers represent the combined features, i.e., both lifetime and intensity parameters together in the classifier. Despite intensity features shown to be good parameters, classification can clearly be improved using both lifetime and intensity features. Furthermore, lifetime parameters showed to be the best features for this set. Lifetime features showed better performance allowing higher sensitivity with high specificity. Table 6.3 summarizes the metrics for each classifier and feature set.

Table 6.3 - Classification metrics for each feature set.

	Lifetime	Intensity	Combined
Sensitivity	0.86	0.57	0.88
Specificity	0.73	0.66	0.67
Accuracy	0.68	0.63	0.73
Precision	0.54	0.50	0.60
F-1 score	0.67	0.53	0.70

Source: By the author.
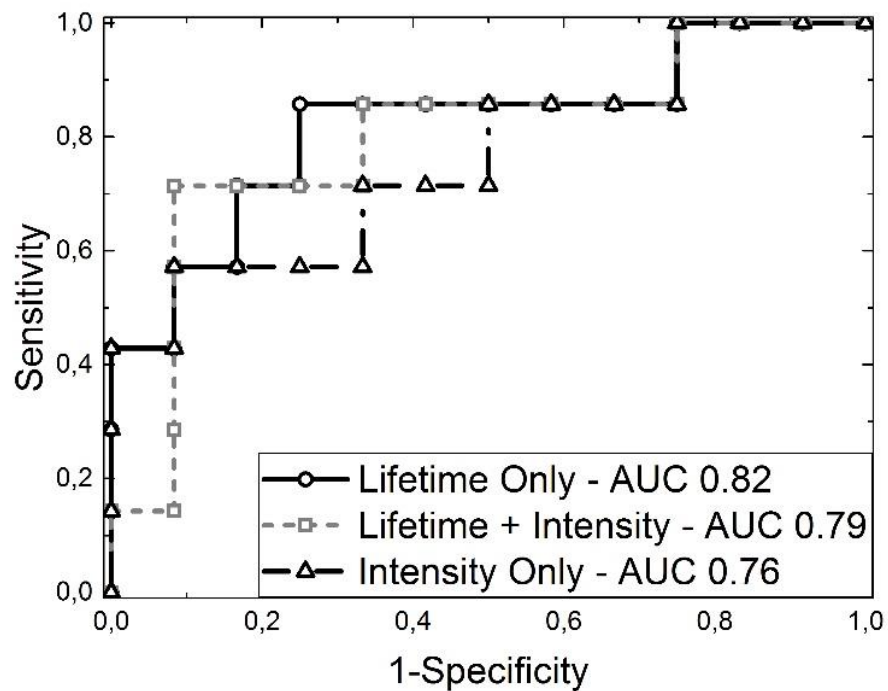
Figure 6.9 -   Classifiers ROC curves and the AUC for Test Set using only Intensity as input (dash black line, triangles markers), both Intensity and Lifetime parameters (dot gray line, square markers), and only lifetime parameters (solid black line, circle markers).
Source: By the author.

6.4 Discussions

This section reports that FLIm dermoscope is capable of fast (acquisition time <2 s), widefield (FOV ~60 mm^2) and label-free skin autofluorescence lifetime imaging at three emission spectral bands simultaneously. As for any diagnostic device, it is important to guarantee that the FLIm system takes reproducible measurements. Generally, all the optical systems need to be calibrated and validated with standard samples before any measurement. Imaging the Chroma® slide standards the system was proved to provide stable measurements during the clinical study time as shown in Figure 6.6 and Table 6.2.

Regarding the instrumentation presented, previous demonstrations of endogenous FLIM imaging systems have been already reported. Multiphoton imaging was reported on *in vivo* and *ex vivo* studies, although this technique can be able to achieve high resolution and deeper tissues, it usually has a limited FOV (usually 200 µm) and has a low speed for acquiring lifetime images for clinical applications (tens of seconds).[77-80] Single-photon lifetime imaging systems were also reported *in vivo* and *ex vivo* studies on other types of tissue, despite some of these studies demonstrates great achievements in FOV and speed, they are still on a benchtop and do not count with multispectral channels.[17-18, 45, 48] Although these reports showed potential results, there is still a lack of human clinical studies.

In the present study, a total of 38 nBCC diagnosed patients were imaged by the FLIm dermoscope (Figure 6.7 (A)). It is important to note that FLIm dermoscopy imaging did not interfere with the tissue biopsy resection procedure scheduled for these patients. The large FOV enabled imaging not only the whole visual extent of the lesions but also surrounding non-involved tissue as shown in Figure 6.7 (B). This feature is relevant for delineating lesion boundaries in the FLIm OB maps, as shown in Figure 6.7 (C). Considering its clinical use, the FLIm dermoscope showed to be robust, no technical problems resulted in decreased system performance. Each imaged tissue site takes less than 3 seconds, so no relevant changes were introduced to the patient appointment. Patients and dermatologists did not have any complaints during the whole study period

It is important to infer that absolute intensity (Figure 6.8 (A-C)), fast-lifetime (Figure 6.8 (M-O)), and slow-lifetime weight (Figure 6.8 (P-R)), present lower values for the lesion region than for the surrounding tissue (p-values lower than 0.001).[81] These results corroborate with trends previously reported using FLIM on *ex vivo* fresh biopsies samples, where fluorescence related to collagen/elastin and NADH channels were studied, showing lower values both for lifetime and intensity when comparing BCC with normal skin. [17-18]

However, lower differences were shown on the average lifetime values. As shown in Figure 6.8. (G-I), the average lifetime values showed compatibility [81] for the first two channels comparing the healthy and lesion sites, presenting different results only on the 3rd channel. These results are also related to previous literature reports, where the same trend was observed in the average lifetime on the shorter and longer wavelengths.[17]

Regarding the slow-lifetime (Figure 6.8 (J-L)) and the fast-lifetime for the 3rd channel Figure 6.8 (O)), the trends shown in the present study show opposite behavior when compared with the *ex vivo* literature reports. However, a clinical study using fluorescence lifetime spectroscopy reported a similar result for these OB. Exciting BCC and normal skin at 378 nm, autofluorescence lifetime of six patients were reported. Despite the lower number of samples, this is the only study on human patients study for comparison using the same spectral range of the NADH and FAD related fluorescence.[82]

More correspondingly results about FAD related emission band were found by Miller *et al.*[13] when investigating SCC. FLIM data were acquired by single-photon excitation at 480 nm and emission at 535 nm in an animal model. Results showed SCC presented lower values for fast-lifetimes and similar values for slow-lifetimes when comparing tumor tissue with healthy skin on the FAD emission range.

Additionally, from Figure 6.8, it is possible to infer that some of the intensity and lifetime features showed an overlap between the distributions of healthy and nBCC. As expected, in features distributions with higher overlaps, the statistical test results showed an uncertainty of difference. However, p-values lower than 0.001 were obtained in three steady-state, and eight lifetime associated features. As shown by the p-values, lifetime associated features carry more information than steady-state associated features, leading to higher classification scores, as shown in Table 6.3 and Figure 6.9. Also, as expected, combined steady-state and lifetime features increased the sensitivity and accuracy of the LDA classifier. It is important to realize that, for higher classification scores, lifetime associated features need to be used as input. Thus, a system without lifetime features would be incomplete.

The results of Figure 6.9 also corroborate with the first demonstration of single-photon FLIM for discriminating between healthy and BCC lesion tissue. It was demonstrated in unfixed human tissue biopsy samples, and both intensity and lifetime features were used as inputs for a simple model.[18] Classification of BCC areas from surrounding uninvolved skin tissue based on autofluorescence lifetimes was significantly more accurate than when using autofluorescence lifetimes (ROC-AUC: ~0.9 for lifetimes vs. ~0.6 for intensities). Although these results were promising, the main limitation of this study was its small sample size (n=38).

6.5 Final remarks

In summary, these section results are based on a small database of FLIm dermoscopy images from 38 patients, all confirmed as nBCC based on biopsy histopathological evaluation. It enabled exploring the potentials of this novel dermoscope to distinguish between healthy and nBCC lesion tissue.

It was demonstrated that the main OB are related to slow lifetime-weight, fast-lifetime, and absolute intensity. The first two of them are related to the lifetime, and the last one is related to the steady-state. In all of these OB nBCC showed lower values than healthy skin.

Using a combination of steady-state and lifetime autofluorescence, FLIm derived features within a linear discriminant analysis statistical classifier, regions of nBCC lesions could be discriminated from surrounding non-involved tissue regions. It is important to note that even within the same dermoscope FOV, encouraging estimated levels of sensitivity (0.88), specificity (0.67), and accuracy (0.73).

These results suggest that FLIm dermoscope has the potential to provide *in situ* delineation of nBCC lesions. Given that surgical excision of malignant skin lesions is the most recommended treatment option and incomplete excision rate is closely dependent on dermatologist's training and experience and can be as high as ~65%. [3-4, 9] A dermatological imaging tool that could provide automated *in situ* delineations of skin malignant lesions would potentially result in a significant increase of complete excision rates and improved the clinical outcomes.

7 PART C: FLIm DERMOSCOPE TO DISTINGUISH BETWEEN MALIGNANT AND BENIGN LESIONS

This section reports the FLIm dermoscope capability of differentiating between clinically similar lesions, as well as between five-classes of malignant and benign lesions. Using the same basis of data processing with the addition of more steps, a more complex approach to data analysis was developed. Moreover, an exploratory analysis on model most important variables, and a comparison between two types of classifiers was performed.

7.1.1 Experimental

7.1.2 FLIm System

The FLIm system used in the following sections of PART C is the same used in PART B (section 6). Image acquisition methods and system parameters were maintained the same, as well as the system stability checks. Laser Safety was also ensured by the same method based on ANSI guidelines as shown in section 6.1.3.

7.1.3 Clinical study

Measurements on human skin lesions were performed to evaluate the system performance to distinguish lesions. All enrolled patients were imaged at the Skin Department, at Hospital Amaral Carvalho (Jahu, SP - Brazil), a cancer hospital. A total of 56 no-pigmented and no-ulcerated nodular and superficial BCC (basal cell carcinoma) lesions (42 patients), 23 SCC (squamous cell carcinoma) lesions (12 patients), 23 Melanoma lesions (18 patients), 25 IN (intradermal nevus) (20 patients), 41 pSK (pigmented seborrheic keratoses) lesions (27 patients), were previously selected and identified by a dermatologist, who also provided a diagnosis based both on clinical evaluation, dermoscopy, and biopsy if necessary. All melanomas and SCCs had the histopathological diagnosis confirmed.

The imaging acquisition protocol followed the same presented in section 6.1.3 and was approved by the Internal Review Board of the Amaral Carvalho Hospital (CAAE:71208817.5.00005434).

7.2 Data Processing

7.2.1 Mask construction

After correcting each pixel temporal vector as shown in section 6.2.1 (temporal vector baseline extraction and correction), it was necessary to create masks to exclude unwanted pixels and to determine the ROI of the image as well as in section 6.2.3 (manual ROI selection). However, a more complex approach was developed in this section. First, a mask was created to exclude probe border pixels, i.e., pixels that are out of the FOV. To do this, a circular binary mask of 70 pixels of radius, centered on the center of the FLIm image was created. Border pixels were then excluded providing a circular image. This mask is shown in Figure 7.1 (A) in a red solid circle. Henceforth, all the pixels out of the circle were taken out of all the calculus.

As well as in section 6.2.3 (manual ROI selection), each image has, in the same field of view, both healthy and abnormal tissues. A mask was then created to distinguish the two regions using the corrected temporal vectors joined with the information of the location of each pixel. Temporal vectors were used because they carry information about both fluorescence intensity and decay behavior, and, as shown in section 6, they can be used to distinguish healthy from abnormal tissue.[70] Additionally, pixel location was used to avoid grouping distant pixels in the same ROI for the mask, since the lesion pixels should be close to each other.

An unsupervised K-Means method [83] was applied using as input both pixel location and temporal vectors to create two groups (healthy and lesion). The method was applied five times after randomization, major distances were chosen as the final groups. Figure 7.1 shows a sample of a mask of lesion region (Figure 7.1 (B)) and healthy surrounding tissue (Figure 7.1 (C)), false colors were applied to a better representation of the image and mask.
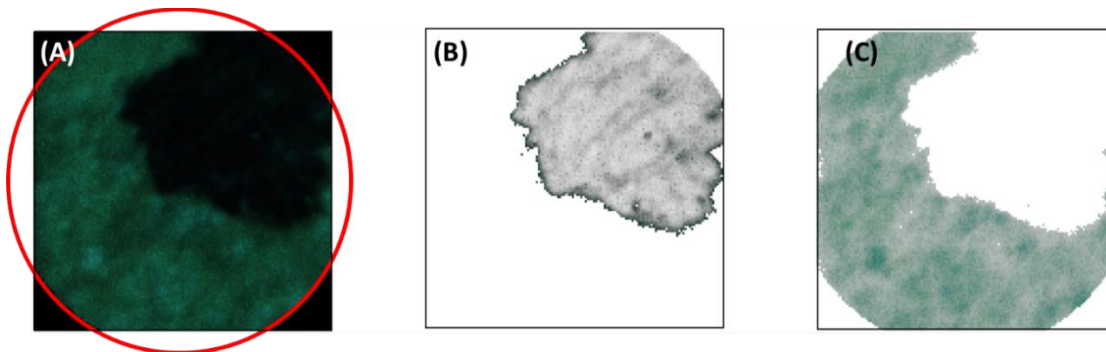
Figure 7.1 - FLIm image mask construction process in false colors. Round mask excludes pixel borders (A), location K-Means mask to distinguish between lesion (B) and healthy tissue (C).
Source: By the author.

7.2.2 Optical Biomarker feature extraction

As well as in section 6.2.2 (OB extraction), temporal vectors were fitted into bi-exponential decays to produce the lifetime parameters, as well as integrated curves to produce the intensity parameters. Since the normalized intensity presented in section 6.2.2 does not demonstrate higher differences between healthy and abnormal tissues (as shown in section 6.3.3), this OB was replaced by the Intensity ratios. These ratios are related to properties described in the literature such as the cellular redox ratio (I_2/I_3) and increase of collagen in (I_1/I_2)[23, 84]. However the last ratio (I_1/I_3) was not described in the literature. Table 7.1 summarizes the OB extracted.

Table 7.1 - Summary of extracted optical biomarkers set.

	Steady-State Fluorescence		Dynamic Fluorescence		
	Integrated intensity	Intensity ratios	Slow lifetime weights	Fast Lifetime	Slow Lifetime
Channel 1	I_1	I_1/I_2	$w_{slow,1}$	$\tau_{fast,1}$	$\tau_{slow,1}$
Channel 2	I_2	I_2/I_3	$w_{slow,2}$	$\tau_{fast,2}$	$\tau_{slow,2}$
Channel 3	I_3	I_3/I_1	$w_{slow,3}$	$\tau_{fast,3}$	$\tau_{slow,3}$

Source: By the author.

7.2.3 Histogram feature extractions

Coupling both information of the mask created with the K-Means method (section 7.2.1), and the calculated OB per pixel (section 7.2.2) it is possible to calculate each of the OB histogram of the selected ROI and then extract the features. Figure 7.2 shows an example of one of the calculated OB histogram. Extracted features are the most probable value, average value, and full-width half maxima (FWHM), represented by the red line, blue line, and orange arrow, respectively. As well as the histogram skewness not represented in this figure.
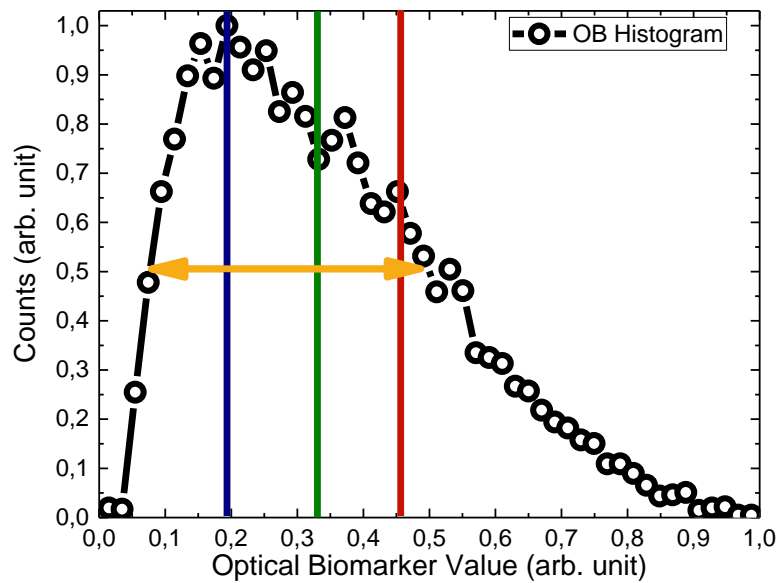
Figure 7.2 -   Example of the extraction of optical biomarkers histogram features. The blue line represents the
mode (most probable value), whereas the green line represents the average value, and the red line
represents the median value. The orange arrow represents the value of full-width half maxima.
Source: By the author.

In this context, each image lesion is turned on a ROI which is itself transformed in a
vector of features extracted from the OB histograms. After all the process each lesion is now
represented by a vector of 75 dimensions instead of 140x140x451 from raw data. Figure 7.3
summarizes the data treatment, where section 6.2.1 (temporal vectors correction) is represented
in blue (A); section 7.2.1 (mask construction) is represented in yellow (B); section 7.2.2 (OB
calculation) is represented in green (C); and section 7.2.3 (histogram feature extraction) is
represented in orange (D). The 75-dimension vector representing each lesion was used as the
input of classifiers.
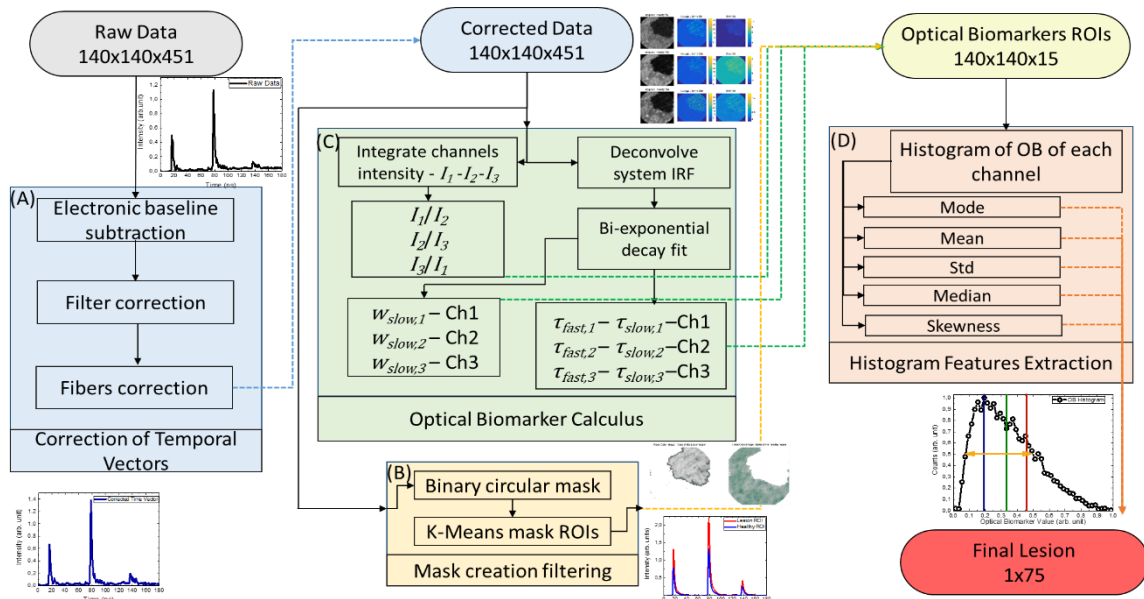
Figure 7.3 - Summary of FLIm image processing. Section 6.2.1 (temporal vectors correction) is represented in blue (A); section 7.2.1 (mask construction) is represented in yellow (B); section 7.2.2 (OB calculation) is represented in green (C); and section 7.2.3 (histogram feature extraction) is represented in orange (D)

Source: By the author.

7.2.4 Supervised classification methods

Labeled samples were randomly divided into the Training set and Test set with 2/3 and 1/3 of the samples respectively (considering the skin conditions and patients to avoid same patient in both sets). For comparison, two methods were used to generate the models, the first one was PLS-DA (partial least squares discriminant analysis), and the second was RF (random forests). PLS-DA was chosen due to its simplicity and interpretability, it is a classification method that uses a supervised principal component analysis to generate a new set of scaled coordinates based on the targets. Then, linear discriminant analysis is performed in the scaled coordinates, and the classification is performed. RF was chosen since it is a well-known robust method for classification, it uses a large number of decision trees that operates as an ensemble. Each tree in the RF has an individual classification, the final class of the RF method takes into account each tree classification vote and the most voted class will be set as the final predicted class.

For PLS-DA eight principal components were cross-validated with the leave-one-out technique for training the model. Whereas for RF, an ensemble of fifty trees was generated. Henceforth, the Test set was used to examine both models' accuracy. Sensitivity, specificity, overall accuracy and AUC of the ROC parameters were calculated to evaluate the performance of the classifiers.

The classification was evaluated in three conditions, the first one by pairs (binary classification) of clinically similar lesions, i.e., nBCC versus IN (non-pigmented), and Melanoma versus pSK (pigmented). Moreover, two-way and five-way classification were performed. In the two-way classification, different types of lesions were grouped and classified between malignant and benign. Whereas in the five-way classification, lesions were classified into five classes, according to the subtype of skin lesion: basal cell carcinoma (BCC); squamous cell carcinoma (SCC); benign nevus (BN); melanoma; and pigmented seborrheic keratosis (pSK). Table 7.2 summarizes the N-way classification methods.

Table 7.2 - Summary of the real labeled diseases for Two-way and Five-way classification.

Two-Way Classification	Five-Way Classification
Malignant	BCC
	SCC
	Melanoma
Benign	Benign Nevus
	pSK

Source: By the author.

7.3 Results

7.3.1 Clinically similar lesions

Since clinically similar skin conditions are challenging researchers and dermatologists, two major classes of similar lesions were chosen to compare the screening accuracy of the present system and the current techniques. To distinguish between IN and nBCC (similar non-pigmented lesions), and pSK and Melanoma (similar pigmented lesions), PLS-DA and RF classifiers' performance were directly compared by their ROC curves (Figure 7.4). Blue solid line represents the PLS-DA classifier performance, whereas the red solid line represents RF classifier performance. When comparing the training set ROC curve of clinically similar lesions (Figure 7.4 (A) and (B)), i.e., nBCC versus IN and Melanoma versus pSK, classifiers methods do not show high differences. However, since high sensitivity is important for cancer diagnostic purposes, PLS-DA shows better performance compared to RF. To evaluate the derived model, a threshold score was chosen to be applied in the test set to classify the malignant lesions with higher sensitivity.
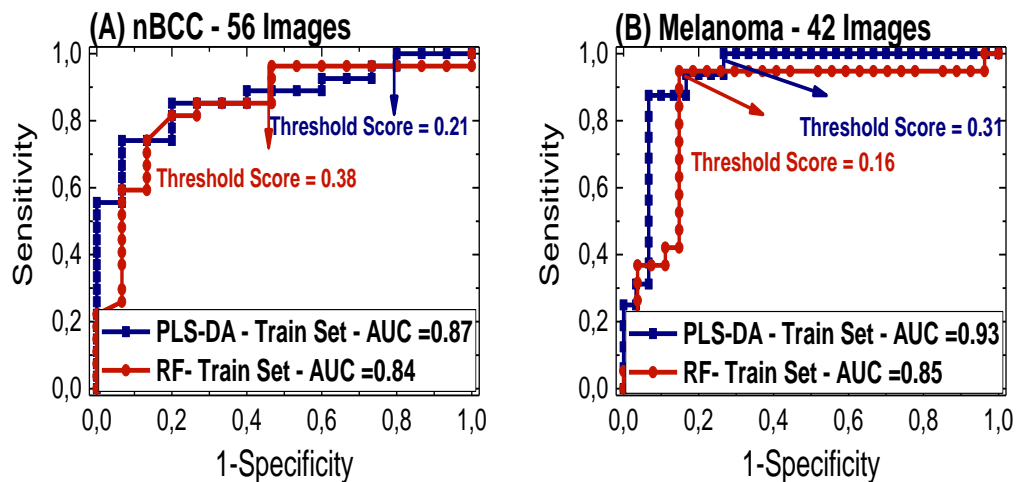
Figure 7.4 -   Comparison of PLS-DA and RF classifiers on Training sets for both nBCC and Melanoma classifications.
Source: By the author.

Aiming 100% of sensitivity on the training set the threshold was specified. Threshold scores for PLS-DA and RF were set to 0.21 and 0.38 for nBCC respectively, whereas for Melanoma the threshold was set to 0.31 and 0.16 respectively.

Table 7.3 shows the classification scores of sensitivity, specificity and overall accuracy for both training and test set. Although having lower overall accuracy, RF showed better performance comparing both methods based on the sensitivity of the test set.

Table 7.3 - Summary of classification algorithms parameters for both lesion, models and sets.

Lesion	Method	Set	Sensitivity	Specificity	Overall Accuracy
nBCC	PLS-DA	Training	1	0.20	0.71
		Test	0.54	0.90	0.71
	RF	Training	0.96	0.46	0.78
		Test	0.82	0.40	0.62
Melanoma	PLS-DA	Training	1	0.73	0.82
		Test	0.82	0.54	0.68
	RF	Training	0.95	0.70	0.80
		Test	1	0.54	0.77

Source: By the author.

First, the nBCC versus IN will be observed to understand the most important features to the classification. As each of the multi-dimensional classifiers has different loadings for each feature and OB, the feature relevance was evaluated and averaged between the models. Then, the most important OB were selected to be shown in each case of the clinically similar lesions. Since channels 1, 2 and 3 are related to collagen/elastin, NADH and FAD fluorescence

respectively, it is possible to relate the features to these optical biomarkers, leading to a better understanding of which features play the key roles for classification.

Figure 7.5 presents distributions of median OB values and their significance calculated by the Mann-Whitney statistical test. To distinguish between nBCC and IN, the major contributions of steady-state fluorescence are in the ratios I_1/I_2, as well as I_2/I_3. Furthermore, the major contributions for dynamics fluorescence are the slow lifetime-weight component (w_{slow}) of the first two channels ($w_{slow,1}$ and $w_{slow,2}$). Moreover, lifetime values also showed important contributions such as the fast and slow lifetime values for channels 2 and 3 ($\tau_{slow,2}$; $\tau_{slow,3}$; $\tau_{fast,2}$; and $\tau_{fast,3}$) (Figure 7.5).

Figure 7.5 - Comparison of major contribution OB features on differentiating IN and nBCC lesions. Green boxplots represent non-malignant nevus, whereas the red boxplots represent the malignant nBCC. * p < 0.05 Mann-Whitney test.
Source: By the author.

Naming these channels to the representative optical biomarkers, it is possible to infer that not only that the ratio of collagen/elastin and NADH, but also the ratio of NADH and FAD have important contributions for distinguishing these skin conditions. The first one showed median values of 0.53 and 0.55 for nBCC and IN respectively, whereas the second one showed median values of 0.30 and 0.32 for nBCC and IN. NADH and FAD ratio is also related to the optical redox ratio, which is a biomarker for cell metabolism. Overall, both ratios show to be lower in the nBCC than IN. Also, as the slow lifetime-weight component can be interpreted as the free fraction of the molecules, Figure 7.5 (C) and (D) demonstrates the difference of both collagen/elastin and NADH related channels.

In general, slow lifetime-weight showed higher values for nBCC than IN, median values of 0.32 and 0.30 for channel 1, whereas for channel 2 the median values were 0.36 and 0.32 for nBCC and IN respectively. Moreover, both for the slow and fast lifetime values, differences can be observed between IN and nBCC. The fast lifetime of NADH related channel show higher values for nBCC (median of 1.16 ns) than for IN (median 1.07 ns) (Figure 7.5 (E)). The slow lifetime of FAD related channel showed median values of 6.09 ns for nBCC and 6.53 ns for IN (Figure 7.5 (F)). Table 7.4 shows the values of the models' most important OB for distinguishing between nBCC and IN.

Table 7.4 - Values of the models' most important OB for nBCC and IN differentiation.

Optical Biomarker	nBCC	IN
I_1/I_2 (arb. units)	0.53	0.55
I_2/I_3 (arb. units)	0.30	0.32
$w_{slow,1}$ (%)	0.32	0.30
$w_{slow,2}$ (%)	0.36	0.32
$\tau_{fast,2}$ (ns)	1.16	1.07
$\tau_{slow,3}$ (ns)	6.09	6.53

Source: By the author.

On the other hand, Figure 7.6 shows the Melanoma versus pSK lesions optimal OB and its statistical significance. As well as for nBCC and IN, NADH/FAD (I_2/I_3) fluorescence ratio was also observed as a major contribution, as well as the slow lifetime-weight of the collagen/elastin ($w_{slow,1}$) related channel, NADH fast lifetime ($\tau_{fast,2}$), and FAD slow lifetime ($\tau_{slow,3}$). However, for Melanoma, other optical biomarkers also demonstrated high importance, such as the fluorescence ratio of collagen/elastin by FAD (I_1/I_3) and the slow lifetime value of NADH ($\tau_{slow,2}$).
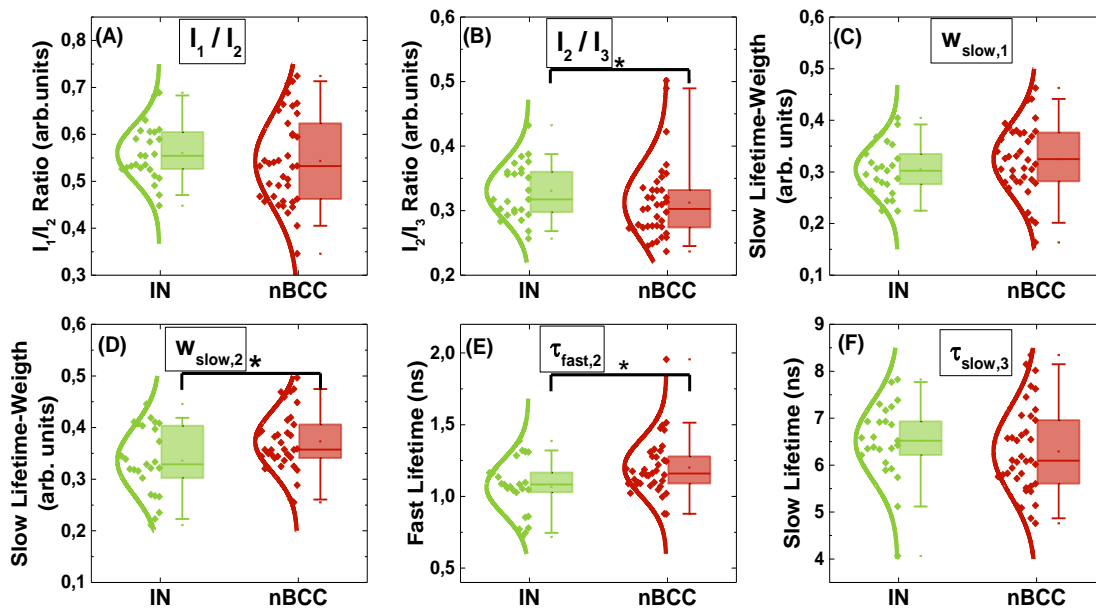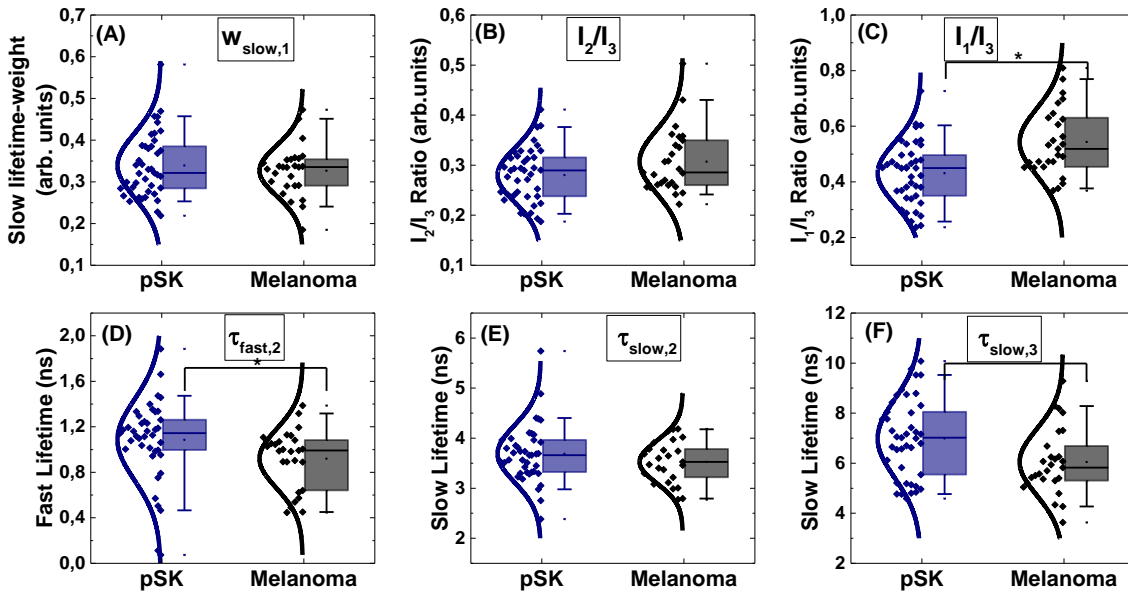
Figure 7.6 - Comparison of major contribution OB features on differentiating pSK and Melanoma lesions. Blue boxplots represent non-malignant pSK, whereas the black boxplots represent the malignant Melanoma. * p< 0.05 Mann-Whitney test.

Source: By the author.

Collagen/elastin related slow lifetime-weight ($w_{slow,1}$) showed median values of 0.34 for melanoma and 0.33 for pSK (Figure 7.6 (A)). Behaviors of increased values for melanoma were found in the ratios of I_2/I_3 and I_1/I_3. Average values of 0.31 and 0.27 were found on the I_2/I_3 ratio for melanoma and pSK respectively.

Whereas for I_1/I_3 ratio, melanoma, and pSK presented median values of 0.52 and 0.45 respectively (Figure 7.6 (B) and (C)). The fast lifetime of channel 2 showed median values of 0.99 ns for melanoma and 1.15 ns for pSK (Figure 7.6 (D)). Whereas slow lifetimes of NADH ($\tau_{slow,2}$) related channel showed values of 3.55 ns and 3.65 ns for melanoma and pSK. FAD related channel slow lifetimes ($\tau_{slow,3}$) showed 5.83 ns and 7.03 ns respectively (Figure 7.6 (E) and (F)).Table 7.5 show the values of the models' most important OB for distinguishing between melanoma and pSK.

Table 7.5 - Values of the models' most important OB for melanoma and pSK differentiation.

Optical Biomarker	Melanoma	pSK
$w_{slow,1}$(%)	0.34	0.33
I_2/I_3(arb. units)	0.31	0.27
I_1/I_3(arb. units)	0.52	0.45
$\tau_{fast,2}$(ns)	0.99	1.15
$\tau_{slow,2}$(ns)	3.55	3.65
$\tau_{slow,3}$ (ns)	5.83	7.03

Source: By the author.

7.3.2 Two-way and five-way Classification

For two-way classification, all the skin classes are split between malignant and benign conditions (as shown in Table 7.2). In this case, both pigmented and non-pigmented lesions were classified together. Training set ROC curves for both PLS-DA and RF are shown in Figure 7.7 (A). For the five-way classification, each group of classes has its own ROC curves, shown in Figure 7.7 (B) and (C), for PLS-DA and RF respectively. In this case line colors represent different skin classes.
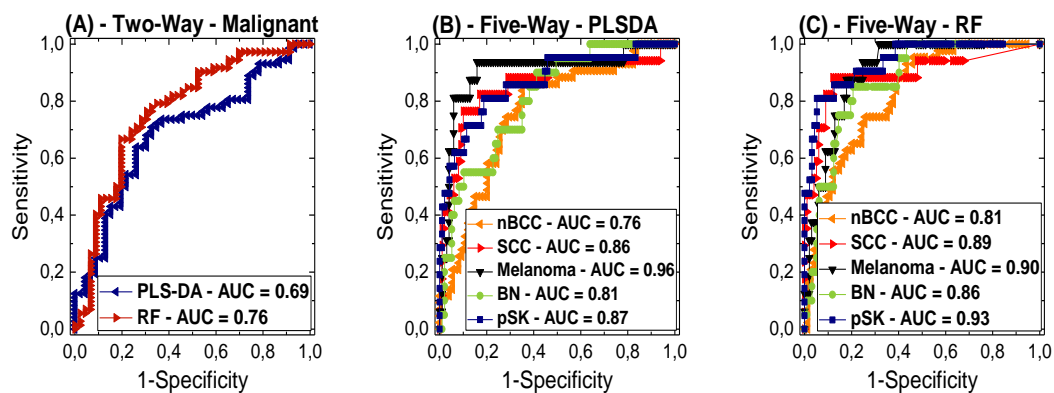
Figure 7.7 - Comparison of PLS-DA and RF classifiers on training sets for both two-way and five-way classifications.
Source: By the author.

Table 7.6 summarizes the scores for each classifier and set. In this case, different from section 7.3.1, the probability threshold for classification was set to the major probability between the classes, e.g., if in five-way classification, the major probability of a lesion is 0.30 in BCC class, it is classified as BCC.

Table 7.6 - Summary of classification parameters for both lesions, models and sets.

N-Way	Sample Set	Classifier	Malignant Average Sensitivity	Malignant Average Specificity	Overall Accuracy	ROC AUC (Average)
Two-Way	Training	PLS-DA	0.59	0.73	0.65	0.70
		RF	0.83	0.54	0.72	0.84
	Test	PLS-DA	0.59	0.70	0.63	0.69
		RF	0.76	0.70	0.72	0.76
Five-Way	Training	PLS-DA	0.72	0.90	0.67	0.85
		RF	0.71	0.85	0.64	0.88
	Test	PLS-DA	0.59	0.84	0.67	0.82
		RF	0.60	0.83	0.60	0.88

Source: By the author.

For data visualization, coordinates generated by each classifier were sorted by cumulative explainability of the model. The first two coordinates of each model in both two-way and five-way classification methods are shown in Figure 7.8, two-way and five-way classification are shown in upper and bottom rows respectively. Whereas the right and left columns of this figure are showing RF (Figure 7.8 (B) and (D)) and PLS-DA (Figure 3.5 (A) and (C)) methods respectively.
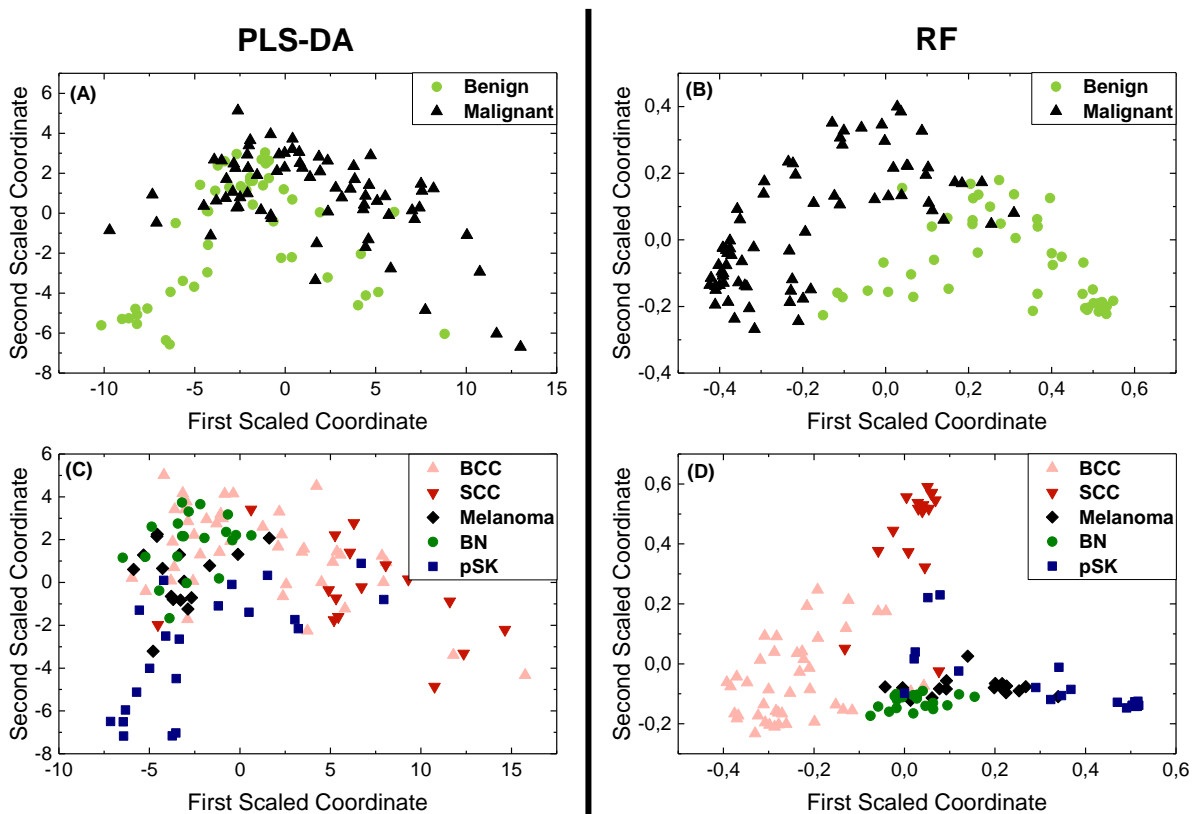
Figure 7.8 -   Visualization of the first and second scaled coordinates of both PLS-DA ((A) and (C)) and RF ((B) and (D)) classifiers. The upper row shows malignant and benign (two-way) classification, whereas the bottom row shows a group of diseases classification (five-way).
Source: By the author.

7.4 Discussion

Skin cancer diagnosis is performed, in general, by three techniques: clinical and physical examination, dermoscopy, and biopsy. Accuracy of these techniques is widely varied according to the type of skin lesion and the dermatologist expertise level.[5-6]

First, regarding NMSC, to distinguish between the clinical similar lesions of nBCC and IN, the FLIm dermoscope showed ROC curves AUC of 0.87 and 0.84 for PLS-DA and RF classifiers respectively (Figure 7.4 (A)). After choosing the proper threshold for the training

set, the test set maximum scores were 0.82 for sensitivity, 0.40 for specificity, and 0.62 for overall accuracy when using the RF classifier (Table 7.3).

Currently, the most common diagnostic technique for NMSC is the clinical and physical examination, sometimes followed by dermoscopy, and rarely followed by a biopsy. In this context, dermatologist sensitivity on clinical and physical inspections vary from 65% to 89%, whereas specificity ranges from 73% to 88%. Dermoscopy can improve the classification results to 73-96% on sensitivity, and 72-91% on specificity. If a biopsy is performed, histopathology overall sensitivity and specificity are around 87% and 94%, respectively. [5, 85]

When comparing these classification parameters with the present in Figure 7.4 and Table 7.3, it is possible to observe a good agreement with the dermoscopy classification levels, being also able to tune the models' threshold to achieve biopsy classification level using the RF classifier (82% sensitivity). At this point, it is important to emphasize that since NMSC is not aggressive, in general, biopsies are not usually taken, since it is time-consuming, expensive, and painful. Furthermore, in developing regions, where there is a lack of dermatologists, materials, and equipment, biopsies are even rarely taken. Under those circumstances, the present study classification levels are notably feasible. As Brazil has a great heterogeneity in cultural, demographic, and socioeconomic conditions, the impacts in the quality of healthcare is very considerable.[29] In particular, to skin cancer disease, the heterogeneous dermatologists distribution leads to a high sub notification, leading to lower treatment rates. In these cases, where a lack of expertise is present, an objective diagnostic method has the potential to decrease the underdiagnosis, especially of the most relevant skin cancer type of melanoma.

Aiming to distinguish between melanoma and pSK (pigmented clinical similar lesions), the classifiers ROC curve AUC were even higher than for BCC as shown in Figure 7.4 (B). On the training set, the PLS-DA classifier achieved 0.93 AUC, whereas the RF classifier achieved AUC of 0.85. Results of classifier scores were calculated after choosing a threshold for better sensitivity and are shown in Table 7.3. On the test set, PLS-DA achieved scores of 0.82 sensitivity, 0.54 specificity, and 0.68 overall accuracy, whereas RF classifier achieved scores of 1 sensitivity, 0.54 specificity, and 0.77 overall accuracy.

Currently, melanoma diagnostics using dermoscopy is also widely used and can improve dermatologist classification accuracy around 50% when compared to clinical examination. Sensitivity ranges from 45-95% and specificity from 45%-98%, being highly dependent on the level of expertise of the dermatologist. When it is possible, biopsies are taken to improve diagnosis due to the potential of metastasis of this type of cancer. In this case, sensitivity and specificities are around 94 % and 85%. [6, 86]

Computer-aided Melanoma diagnosis has been widely developed to improve the diagnosis. Several algorithms have already been used, such as CART, logistic regressions (LR), discriminant analysis, decision trees (DT), SVM, KNN, and deep neural networks. [51-52, 86] These methods were applied using many types of optical devices, such as OCT, scanning laser microscopy, multispectral imaging, white-light, and dermoscopy images.[51] Altogether, previously reported computer-aided Melanoma diagnosis was capable of achieving 51-100% sensitivity and 70-100% specificity, with accuracy ranging from 66-94% [50-51, 87-88].

As well as for BCC, the present work could provide a melanoma classification level similar not only to the current techniques of dermoscopy and biopsy (with proper threshold), but also to previous studies, as shown in Figure 7.4 and Table 7.3 In essence, regarding clinically similar lesions, the present study was clearly able to provide a machine learning-based strategy for skin cancer screening.

Since the present FLIm technique aimed at the endogenous fluorophores fluorescence lifetime to distinguish the lesions, it is important to understand the role of each of the lifetime or steady-state components to the differentiation. Due to the huge variation between the patients' skin lesions' metabolic conditions, there are overlaps on the OB's distributions between the classes, as shown in Figure 7.5 and in Figure 7.6. Thus, with p-values higher than 0.05, a multivariate analysis is usually needed for discriminating the lesions. Some previous studies also compared autofluorescence lifetimes parameters both from NMSC, melanoma, benign lesions, and healthy skin. [16-18, 40, 47, 82, 89-90] Nevertheless, there is a lack of clinical studies comparing benign to malignant lesions. [82]

For NMSC, Figure 7.5 demonstrates the differences in some of the most important features of the models. Regarding lifetime associated OB, there is an increase in $\tau_{fast,2}$ and $w_{slow,2}$ when comparing BCC to IN. Furthermore, BCC showed an I_2/I_3 intensity ratio decreased in relation to IN, which can be interpreted as being similar to the optical redox ratio. To the present author's knowledge, there is only one clinical study comparing BCC to a benign lesion. It reports a spectroscopy lifetime device exciting tissue at 378 nm and acquiring at emission bands related to the NADH and FAD. It also reports that the average lifetime of BCC is lower than the hypochromic nevus (benign lesion) in the NADH channel, whereas the opposite behavior is demonstrated at the FAD channel. [82]

Moreover, for *ex vivo* analysis, other studies were performed. Exciting samples at 393 nm, a comparison of fresh biopsies of human BCC and non-pigmented seborrheic keratosis reported average lifetime values higher for BCC compared to the benign lesion.[17] A FLIM analysis of freshly excised skin lesions was reported using excitation on 760 nm compared

samples of nBCC and dysplasic nevus. Two spectral channels were acquired (380 – 500 nm and 500- 640 nm). Both NADH and FAD related channels average lifetimes showed a higher value for nBCC compared with dysplasic nevus.[80] This shows that depending on the excitation wavelength, channel of acquisition, and type of benign lesion compared, the trend on the average lifetime values can be very different. However, none of the reported studies presented a significant amount of clinical data, the present work analyzed a total of 81 lesions of BCC and IN.

For the comparison between melanoma and pSK, the main FLIm OB features (p-value < 0.05) were I_1/I_3, $\tau_{fast,2}$, and $\tau_{slow,3}$. In the first one, indicating the ratio between the fluorescence intensity of collagen/elastin and FAD, melanoma showed higher values. Regarding the lifetimes, both on NADH and FAD related channels, melanoma showed lower values than pSK. Even in the lifetime associated features with a p-value lower than 0.05 melanoma showed lower values, as shown in Figure 7.6. Furthermore, even with a big overlap and a p-value lower than 0.05, the OB I_2/I_3 results demonstrated to be slightly higher for melanoma than pSK, conversely to the nBCC versus IN behavior previously shown.

Previous studies reported the autofluorescence average lifetime values higher for melanoma when compared with pSK or naevi lesions in human fresh biopsies. [17, 90] Regarding the OB associated with the redox ratio (I_2/I_3), there are several literature reports on *in vitro* cells studies showing lower redox ratios for cancer cells compared to healthy cells, however, to the best of our knowledge there is no clinical study report to compare the results shown in Figure 7.6. It is still important to emphasize that the maximum number of samples in these reports is thirty-seven, whereas the present work compared a total of 64 lesions.

To improve the number of samples, and study the potential to distinguish different skin classes, the two-way and five-way classification were performed, and the results are shown in Figure 7.7, Figure 7.8 and Table 7.6. Using 168 skin conditions images, two-way and five-way classification, ROC-AUC achieved values of 0.69 to 0.96 (Figure 7.7). A visualization of the potential of different class screening of the models is shown in Figure 7.8.

On the test set, as shown in Table 7.6, PLS-DA classifier achieved average malignant sensitivity and specificity of 0.59 and 0.70 in two-way classification, and 0.59 and 0.84 on five-way classification. Evaluating the same scores for RF classifier, average malignant sensitivity and specificity were 0.76 and 0.70 for two-way, and 0.60 and 0.83 for the five-way classification. Overall accuracies for two-way classification were 0.63 and 0.70 for PLS-DA and RF, respectively. Whereas for the Five-way classification, overall accuracies were 0.67 and 0.60 for PLS-DA and RF, respectively.

Similarly, recent work demonstrated that dermatologists' overall accuracy in three-way and nine-way classification tasks was around 66% and 55%, respectively.[52] Being the three-way classification among benign, malignant, and non-neoplasic lesions. Whereas the nine-way classification task involved cutaneous lymphoma and lymphoid infiltrates, benign dermal, malignant dermal, benign epidermal, pre-malignant and malignant epidermal, genodermatoses and supernumerary growths, inflammatory conditions, benign melanocytic lesions, and malignant melanoma classes. Moreover, for comparison with computer-aided diagnosis, it used a convolutional neural networks approach on more than a million skin lesion images. They were able to achieve an overall accuracy of 72.1% and 55.4% for three-way and nine-way classification tasks, respectively.[52]

Given these points, with the two-way and five-way classification overall accuracy of around 70% and 60%, the present work results showed a good agreement when compared to dermatologists' level of classification.

7.5 Final remarks

In conclusion, this section results are based on 168 FLIm dermoscopy images. All melanoma and SCC lesions were confirmed based on biopsy histopathological evaluation, and some of pSK, IN and BCC were confirmed by both visual inspection and biopsy. This clinical study enabled exploring the potentials of the FLIm dermoscope and the generated features to distinguish between benign and malignant lesions. Using a combination of steady-state and lifetime features extracted from native optical biomarkers were used as input to the PLS-DA and the RF classifier. It was possible to distinguish between pigmented and non-pigmented clinical similar lesions with overall accuracies of 71% and 77% respectively. Such a result is pretty similar to the non-trained dermatologist's accuracy level. Regarding sensitivity, it was demonstrated that the FLIm system can be tuned to achieve 100% sensitivity despite losing specificity.

Furthermore, the two-way and five-way classification demonstrated the potential of the extracted features to distinguish between the skin lesions. Classifiers showed an overall accuracy of 70% in the two-way and 60% in five-way classifications. Given that dermatologists without biopsy have accuracies of around 66% in three-way classification (benign, malignant and non-neoplasic)[52], a dermatological tool that could provide automated *in situ* diagnosis with similar accuracy would potentially result in increased success in the clinical outcomes, especially in sites where there is a lack of dermatology expertise.

8 CONCLUSION

Aiming to develop strategies for skin cancer screening, the present study investigated the metabolic conditions of different cell types and evaluated a portable multispectral fluorescence lifetime device.

In essence, it was observed that the intracellular co-enzymes are powerful natural optical biomarkers to access metabolic conditions. Lower values of optical redox ratio are related to higher metabolic activity, thus, it can be a marker for cancer cells. In likely manner, lower autofluorescence lifetimes can be a biomarker for glycolysis, and hence for higher metabolic activity of cancer cells. It is important to emphasize that for not only the average lifetimes but the slow and fast lifetimes as well as the lifetime weights (protein-bound and free fraction) can be used to distinguish among the cells.

The clinical study on 119 patients demonstrated that lifetime associated parameters demonstrated to be as important as steady-state fluorescence, and combining the two techniques gives powerful results. It was possible to distinguish between healthy and nBCC tissue with a sensitivity of 0.88, a specificity of 0.67, and an accuracy of 0.73. Despite the modest accuracy, this model is still compatible with the dermatologists' accuracy, since the higher tumor excision recurrence rates (up to 65 %).[70]

The developed machine learning models were able to distinguish pigmented (melanoma and pSK) and non-pigmented (nBCC and IN) clinically similar lesions, which are very challenging to dermatologists with accuracies higher than 70%. It was also possible to tune the models to achieve 100% sensitivity (and loose specificity). These results are very similar to the dermatologists' accuracy level when using dermoscopy (70-91 %) and biopsy (87-94 %) techniques.

Furthermore, models also demonstrated to be powerful to distinguish between five types of lesions, BCC, SCC and melanoma (malignant), and pSK and IN (benign). Accuracies for two-way and five-way classification were around 70 % and 60% respectively, such a result is very promising since dermatologists' accuracy is around 66% for three-way classification.

The central hypothesis of this work, that metabolism-based diagnosis could be performed with endogenous fluorescence, was proven using machine learning techniques. A scientific gap of clinical studies on skin cancer diagnosis using autofluorescence lifetime was also fulfilled, showing this technique as a powerful tool for screening skin cancer. In addition, considering the dermatologists distribution in Brazil, this technique can be a powerful tool to avoid skin cancer misdiagnosis.

REFERENCES

1 SIEGEL, R. L.; MILLER, K. D.; JEMAL, A. Cancer statistics, 2019. **CA**: a cancer journal for clinicians, v. 69, n. 1, p. 7–34, Jan. 2019.

2 INSTITUTO NACIONAL DO CÂNCER. **Estimativa 2018**: incidência de câncer no Brasil. estimativa 2018: incidência de câncer no Brasil / Instituto Nacional de Câncer José Alencar Gomes da Silva. Coordenação de Prevenção e Vigilância. – Rio de Janeiro: INCA, 2017. Available from: http://www1.inca.gov.br/estimativa/2018/estimativa-2018.pdf. Accessible at: 29 Nov. 2019.

3 ALAIBAC, M. Facial basal cell carcinoma: analysis of recurrence and follow-up strategies. **Oncology Reports**, v. 26, n. 6, p. 1423–1429, Sept. 2011.

4 GRELCK, K. *et al*. Incidence of residual nonmelanoma skin cancer in excisions after shave biopsy. **Dermatologic Surgery**, v. 39, n. 3 Part 1, p. 374–380, 1 Mar. 2013.

5 MOGENSEN, M.; JEMEC, G. B. E. Diagnosis of nonmelanoma skin cancer/keratinocyte carcinoma: a review of diagnostic accuracy of nonmelanoma skin cancer diagnostic tests and technologies. **Dermatologic Surgery**, v. 33, n. 10, p. 1158–1174, Oct. 2007.

6 KITTLER, H. *et al*. Diagnostic accuracy of dermoscopy. **Lancet Oncology**, v. 3, n. 3, p. 159–165, Mar. 2002.

7 MASSONE, C.; DI STEFANI, A.; SOYER, H. P. Dermoscopy for skin cancer detection. **Current Opinion in Oncology**, v. 17, n. 2, p. 147–153, Mar. 2005.

8 QADIR, M. I. Skin cancer: etiology and management. **Pakistan Journal of Pharmaceutical Sciences**, v. 29, n. 3, p. 999–1003, May 2016.

9 HOLMKVIST, K. A.; ROGERS, G. S.; DAHL, P. R. Incidence of residual basal cell carcinoma in patients who appear tumor free after biopsy. **Journal of the American Academy of Dermatology**, v. 41, n. 4, p. 600–605, Oct. 1999.

10 APPLEGATE, M. B.; ROBLYER, D. High-speed spatial frequency domain imaging with temporally modulated light. **Journal of Biomedical Optics**, v. 22, n. 7, p. 76019, July 2017.

11 STRINGARI, C. *et al*. Multicolor two-photon imaging of endogenous fluorophores in living tissues by wavelength mixing. **Scientific Reports**, v. 7, n. 1, p. 3792, Dec. 2017.

12 KOLENC, O. I.; QUINN, K. P. Evaluating cell metabolism through autofluorescence imaging of NAD(P)H and FAD. **Antioxidants & Redox Signaling**, v. 30, n. 6, p. 875–889, Feb. 2019.

13 MILLER, J. P. *et al*. Multimodal fluorescence molecular imaging for *in vivo* characterization of skin cancer using endogenous and exogenous fluorophores. **Journal of Biomedical Optics**, v. 22, n. 6, p. 066007, June 2017.

14 TENG, F. *et al*. Wearable near-infrared optical probe for continuous monitoring during breast cancer neoadjuvant chemotherapy infusions. **Journal of Biomedical Optics**, v. 22, n.

1, p. 014001, Jan. 2017.

15 BRANCALEON, L. *et al*. In vivo Fluorescence Spectroscopy of Nonmelanoma Skin Cancer¶. **Photochemistry and Photobiology**, v. 73, n. 2, p. 178, May 2001.

16 MUNRO, I. *et al*. Toward the clinical application of time-domain fluorescence lifetime imaging. **Journal of Biomedical Optics**, v. 10, n. 5, p. 051403, Sept-Oct., 2005.

17 DE BEULE, P. A. A. *et al*. A hyperspectral fluorescence lifetime probe for skin cancer diagnosis. **Review of Scientific Instruments**, v. 78, n. 12, p. 123101, Dec. 2007.

18 GALLETLY, N. P. *et al*. Fluorescence lifetime imaging distinguishes basal cell carcinoma from surrounding uninvolved skin. **British Journal of Dermatology**, v. 159, n. 1, p. 152–161, July 2008.

19 NA, R.; STENDER, I.-M.; WULF, H. C. Can autofluorescence demarcate basal cell carcinoma from normal skin? a comparison with protoporphyrin IX fluorescence. **Acta Dermato-Venereologica**, v. 81, n. 4, p. 246–249,Sept. 2001.

20 GORPAS, D. *et al.* Autofluorescence lifetime augmented reality as a means for real-time robotic surgery guidance in human patients. **Scientific Reports**, v. 9, n. 1, p. 1187, Dec. 2019.

21 HEIKAL, A. A. Intracellular coenzymes as natural biomarkers for metabolic activities and mitochondrial anomalies. **Biomarkers in Medicine**, v. 4, n. 2, p. 241–263,Apr. 2010.

22 SHI, L. *et al.* Label-free fluorescence spectroscopy for detecting key biomolecules in brain tissue from a mouse model of Alzheimer's disease. **Scientific Reports**, v. 7, n. 1, p. 2599, Dec. 2017.

23 LIU, Z. *et al.* Mapping metabolic changes by noninvasive, multiparametric, high-resolution imaging using endogenous contrast. **Science Advances**, v. 4, n. 3, p. eaap9302, Mar. 2018.

24 POULI, D. *et al*. Imaging mitochondrial dynamics in human skin reveals depth- dependent hypoxia and malignant potential for diagnosis. **Science Translational Medicine**, v. 8, n. 367, p. 367ra169-367ra169, Nov. 2017.

25 BIGIO, I. J.; MOURANT, J. R. Ultraviolet and visible spectroscopies for tissue diagnostics: fluorescence spectroscopy and elastic-scattering spectroscopy. **Physics in Medicine and Biology**, v. 42, n. 5, p. 803–814, May1997.

26 GREENLEE, R. T. *et al*. Cancer statistics, 2000. **CA**: a cancer journal for clinicians, v. 50, n. 1, p. 7–33, Jan. 2000.

27 RAMYA SILPA, S. A review on skin cancer. **International Research Journal of Pharmacy**, v. 4, n. 8, Aug. 2013. DOI: 10.7897 / 2230-8407.04814.

28 FINK, C.; HAENSSLE, H. A. Non-invasive tools for the diagnosis of cutaneous melanoma. **Skin Research and Technology**, v. 23, n. 3, p. 261–271, Aug. 2017.

29 BUZZÁ, H. H. *et al*. Overall results for a national program of photodynamic therapy for basal cell carcinoma: a multicenter clinical study to bring new techniques to social health

care. **Cancer Control**, v. 26, n. 1, p. 107327481985688, Jan. 2019.

30 RICHARDS-KORTUM, R. *et al*. A model for extraction of diagnostic information from laser induced fluorescence spectra of human artery wall. **Spectrochimica Acta Part A:** molecular spectroscopy, v. 45, n. 1, p. 87–93, Jan. 1989.

31 RICHARDS-KORTUM, R. *et al*. Spectroscopic diagnosis of colonic dysplasia. **Photochemistry and Photobiology**, v. 53, n. 6, p. 777–786, June 1991.

32 VO-DINH, T. *et al*. In vivo cancer diagnosis of the esophagus using differential normalized fluorescence (DNF) indices. **Lasers in Surgery and Medicine**, v. 16, n. 1, p. 41–47, Jan. 1995.

33 BEUTHAN, J.; MINET, O.; MÜLLER, G. Observations of the fluorescence response of the coenzyme NADH in biological samples. **Optics Letters**, v. 18, n. 13, p. 1098, July 1993.

34 ANDERSSON-ENGELS, S. *et al*. Fluorescence imaging and point measurements of tissue: applications to the demarcation of malignant tumors and atherosclerotic lesions from normal tissue. **Photochemistry and Photobiology**, v. 53, n. 6, p. 807–814, June 1991.

35 SCHWARZ, R. A. *et al*. Noninvasive evaluation of oral lesions using depth-sensitive optical spectroscopy. **Cancer**, v. 115, n. 8, p. 1669–1679, Apr. 2009.

36 ALHALLAK, K. *et al*. Optical redox ratio identifies metastatic potential-dependent changes in breast cancer cell metabolism. **Biomedical Optics Express**, v. 7, n. 11, p. 4364, Nov. 2016.

37 LAKOWICZ, J. R. **Principles of fluorescence spectroscopy**. New York: Springer, 2006.

38 JYOTHIKUMAR, V.; SUN, Y.; PERIASAMY, A. Investigation of tryptophan–NADH interactions in live human cells using three-photon fluorescence lifetime imaging and Förster resonance energy transfer microscopy. **Journal of Biomedical Optics**, v. 18, n. 6, p. 060501, June 2013.

39 SINSUEBPHON, N. *et al*. Comparison of illumination geometry for lifetime-based measurements in whole-body preclinical imaging. **Journal of Biophotonics**, v. 11, n. 10, p. e201800037, Oct. 2018.

40 MCGINTY, J. *et al*. Wide-field fluorescence lifetime imaging of cancer. **Biomedical Optics Express**, v. 1, n. 2, p. 627, Sept. 2010.

41 SHRESTHA, S. *et al*. High-speed multispectral fluorescence lifetime imaging implementation for in vivo applications. **Optics letters**, v. 35, n. 15, p. 2558–60, Aug. 2010.

42 PARK, J. *et al*. Biochemical characterization of atherosclerotic plaques by endogenous multispectral fluorescence lifetime imaging microscopy. **Atherosclerosis**, v. 220, n. 2, p. 394–401, Feb. 2012.

43 BEC, J. *et al*. In vivo label-free structural and biochemical imaging of coronary arteries using an integrated ultrasound and multispectral fluorescence lifetime catheter system. **Scientific Reports**, v. 7, n. 1, p. 8960, Dec. 2017.

44 SUN, Y. *et al.* Simultaneous time- and wavelength-resolved fluorescence spectroscopy for near real-time tissue diagnosis. **Optics Letters**, v. 33, n. 6, p. 630, Mar. 2008.

45 CHENG, S. *et al*. Flexible endoscope for continuous in vivo multispectral fluorescence lifetime imaging. **Optics letters**, v. 38, n. 9, p. 1515–7, 2013.

46 CHENG, S. *et al*. In Vivo Detection of Oral Epithelial Pre-Cancer and Cancer by Endogenous Fluorescence Lifetime Imaging (FLIM) Endoscopy. *In*: BIOMEDICAL OPTICS 2016. Washington. **Anais[**...] Washington, D.C.: OSA, 2016

47 PIRES, L. *et al*. Time-resolved fluorescence lifetime for cutaneous melanoma detection. **Biomedical Optics Express**, v. 5, n. 9, p. 3080, Sept. 2014.

48 CHENG, S. *et al*. Handheld multispectral fluorescence lifetime imaging system for in vivo applications. **Biomedical Optics Express**, v. 5, n. 3, p. 921, Mar. 2014.

49 SCHINDEWOLF, T. *et al*. Classification of melanocytic lesions with color and texture analysis using digital image processing. **Analytical and Quantitative Cytology and Histology**, v. 15, n. 1, p. 1–11, Feb. 1993.

50 BURRONI, M. *et al*. Melanoma computer-aided diagnosis. **Clinical Cancer Research**, v. 10, n. 6, p. 1881–1886, Mar. 2004.

51 MASOOD, A.; ALI AL-JUMAILY, A. Computer aided diagnostic support system for skin cancer: a review of techniques and algorithms. **International Journal of Biomedical Imaging**, v. 2013, p. 1–22, Dec. 2013.

52 ESTEVA, A. *et al.* Dermatologist-level classification of skin cancer with deep neural networks. **Nature**, v. 542, n. 7639, p. 115–118, Feb. 2017.

53 PREMALADHA, J.; RAVICHANDRAN, K. S. Novel approaches for diagnosing melanoma skin lesions through supervised and deep learning algorithms. **Journal of Medical Systems**, v. 40, n. 4, p. 96, Apr. 2016.

54 UCDAVIS CHEMWIKI. **ELECTRONIC spectroscopy**: theory. Available from: http://chemwiki.ucdavis.edu/Physical_Chemistry/Spectroscopy/Electronic_Spectroscopy/Electronic_Spectroscopy%253A_Theory. Acessible at: 20 Dec. 2019.

55 SEMWOGERERE, D.; WEEKS, E. R. Confocal microscopy. *In*: WNEK, G. E.; BOWLIN, G. L. (ed.). **Encyclopedia of biomaterials and biomedical engineering**, 2005. p. 1–10.

56 PAWLEY, J. B. **Handbook of biological confocal microscopy**. New York: Plenum Press, 1995.

57 CROCE, A. C.; BOTTIROLI, G. Autofluorescence spectroscopy and imaging: a tool for biomedical research and diagnosis. **European Journal of Histochemistry**, v. 58, n. 4, Dec. 2014.

58 COUSSENS, L. M.; WERB, Z. Inflammation and cancer. **Nature**, v. 420, n. 6917, p. 860–867, Dec. 2002.

59 ABU-MOSTAFA, Y. S.; MAGDON-ISMAIL, M.; LIN, H.-T. **Learning from data**. New York: AMLBook, 2012. v. 4

60 BISHOP, C. M. *et al.* **Pattern recognition and machine learning**. Berlin: Springer, 2006.

61 TOPOL, E. J. High-performance medicine: the convergence of human and artificial intelligence. **Nature Medicine**, v. 25, n. 1, p. 44–56, Jan. 2019.

62 SKALA, M. C. *et al.* In vivo multiphoton microscopy of NADH and FAD redox states, fluorescence lifetimes, and cellular morphology in precancerous epithelia. **Proceedings of the National Academy of Sciences**, v. 104, n. 49, p. 19494–19499, Dec. 2007.

63 KUZNETSOV, A. V.; MARGREITER, R. Heterogeneity of mitochondria and mitochondrial function within cells as another level of mitochondrial complexity. **International Journal of Molecular Sciences**, v. 10, n. 4, p. 1911–1929, Apr. 2009.

64 PAVLOVA, I. *et al.* Understanding the biological basis of autofluorescence imaging for oral cancer detection: high-resolution fluorescence microscopy in viable tissue. **Clinical Cancer Research**, v. 14, n. 8, p. 2396–2404, Mar. 2008.

65 LIBERTI, M. V; LOCASALE, J. W. The Warburg effect: how does it benefit cancer cells? **Trends in Biochemical Sciences**, v. 41, n. 3, p. 211–218, Mar. 2016.

66 DRUZHKOVA, I. N. et al. The metabolic interaction of cancer cells and fibroblasts – coupling between NAD(P)H and FAD, intracellular pH and hydrogen peroxide. **Cell Cycle**, v. 15, n. 9, p. 1257–1266, May 2016.

67 BIRD, D. K. *et al.* Metabolic mapping of MCF10A human breast cells via multiphoton fluorescence lifetime imaging of the coenzyme NADH. **Cancer Research**, v. 65, n. 19, p. 8766–8773, Oct. 2005.

68 SKALA, M. C. *et al.* In vivo multiphoton fluorescence lifetime imaging of protein-bound and free nicotinamide adenine dinucleotide in normal and precancerous epithelia. **Journal of Biomedical Optics**, v. 12, n. 2, p. 024014, Mar-Apr. 2007.

69 SKALA, M. C. *et al.* In vivo multiphoton fluorescence lifetime imaging of protein-bound and free nicotinamide adenine dinucleotide in normal and precancerous epithelia. **Journal of Biomedical Optics**, v. 12, n. 2, p. 24014, Mar-Apr. 2007.

70 ROMANO, R. A. *et al.* Multispectral autofluorescence dermoscope for skin lesion assessment. **Photodiagnosis and Photodynamic Therapy**, v. 30, p. 101704, June 2020.

71 ROSA, R. G. T. **Assembly, characterization, and validation of a fluorescence lifetime rigid endoscope for clinical imaging of skin lesions**. 2018. 98 p. Tese (Doutorado em Ciências) - Instituto de Física de São Carlos, Universidade de São Paulo, São Carlos, 2018.

72 MALIK, B. H. *et al.* Objective detection of oral carcinoma with multispectral fluorescence lifetime imaging *In Vivo*. **Photochemistry and Photobiology**, v. 92, n. 5, p. 694–701, Sept. 2016.

73 AMERICAN NATIONAL STANDARD **American National Standard for Safe Use of Lasers**. 2007. Available from: https://eliceirilab.org/sites/default/files/2017-

04/American%20National%20Standard%20for%20Safe%20Use%20of%20Lasers.pdf. Accessible at: 23 jan. 2019.

74 BLACKER, T. S.; DUCHEN, M. R. Investigating mitochondrial redox state using NADH and NADPH autofluorescence. **Free Radical Biology and Medicine**, v. 100, p. 53–65, Nov. 2016.

75 XYLAS, J. *et al.* Noninvasive assessment of mitochondrial organization in three-dimensional tissues reveals changes associated with cancer development. **International Journal of Cancer**, v. 136, n. 2, p. 322–332, Jan. 2015.

76 GLAS, A. S. *et al.* The diagnostic odds ratio: a single indicator of test performance. **Journal of Clinical Epidemiology**, v. 56, n. 11, p. 1129–1135, Nov. 2003.

77 SANCHEZ, W. Y. *et al.* Changes in the redox state and endogenous fluorescence of in vivo human skin due to intrinsic and photo-aging, measured by multiphoton tomography with fluorescence lifetime imaging. **Journal of Biomedical Optics**, v. 18, n. 6, p. 061217, Nov. 2012.

78 SANCHEZ, W. Y. *et al.* Analysis of the metabolic deterioration of ex vivo skin from ischemic necrosis through the imaging of intracellular NAD(P)H by multiphoton tomography and fluorescence lifetime imaging microscopy. **Journal of Biomedical Optics**, v. 15, n. 4, p. 046008, July-Aug. 2010.

79 BENATI, E. *et al.* Quantitative evaluation of healthy epidermis by means of multiphoton microscopy and fluorescence lifetime imaging microscopy. **Skin Research and Technology**, v. 17, n. 3, p. 295–303, Aug. 2011.

80 PATALAY, R. *et al.* Quantification of cellular autofluorescence of human skin using multiphoton tomography and fluorescence lifetime imaging in two spectral detection channels. **Biomedical Optics Express**, v. 2, n. 12, p. 3295, Dec. 2011.

81 AMRHEIN, V.; GREENLAND, S.; MCSHANE, B. Scientists rise up against statistical significance. **Nature**, v. 567, n. 7748, p. 305–307, Mar. 2019.

82 SAITO NOGUEIRA, M. *et al.* Portable fluorescence lifetime spectroscopy system for in-situ interrogation of biological tissues. **Journal of Biomedical Optics**, v. 22, n. 12, p. 1, Oct. 2017.

83 BOTTOU, L.; BENGIO, Y. Convergence properties of the K-Means algorithm. 1995. Available from: https://papers.nips.cc/paper/989-convergence-properties-of-the-k-means-algorithms.pdf. Accessible at 30 Apr. 2019.

84 KALLURI, R.; ZEISBERG, M. Fibroblasts in cancer. **Nature Reviews Cancer**, v. 6, n. 5, p. 392–401, May 2006.

85 COOPER, S. M.; WOJNAROWSKA, F. The accuracy of clinical diagnosis of suspected premalignant and malignant skin lesions in renal transplant recipients. **Clinical and Experimental Dermatology**, v. 27, n. 6, p. 436–438, Sept. 2002.

86 ROSADO, B. Accuracy of computer diagnosis of melanoma. **Archives of Dermatology**, v. 139, n. 3, p. 361, June 2003.

87 KOROTKOV, K.; GARCIA, R. Computerized analysis of pigmented skin lesions: a review. **Artificial Intelligence in Medicine**, v. 56, n. 2, p. 69–90, Oct. 2012.

88 PATHAN, S.; PRABHU, K. G.; SIDDALINGASWAMY, P. C. Techniques and algorithms for computer aided diagnosis of pigmented skin lesions—a review. **Biomedical Signal Processing and Control**, v. 39, p. 237–262, Jan. 2018.

89 CHEN, B. *et al*. Support vector machine classification of nonmelanoma skin lesions based on fluorescence lifetime imaging microscopy. **Analytical Chemistry**, v. 91, n. 16, p. 10640–10647, Aug. 2019.

90 DIMITROW, E. *et al.* Spectral fluorescence lifetime detection and selective melanin imaging by multiphoton laser tomography for melanoma diagnosis. **Experimental Dermatology**, v. 18, n. 6, p. 509–515, June 2009.

ANNEX A – Research Ethics Committee approval

HOSPITAL AMARAL CARVALHO / FUNDAÇÃO DR. AMARAL CARVALHO

PlataForma Brasil
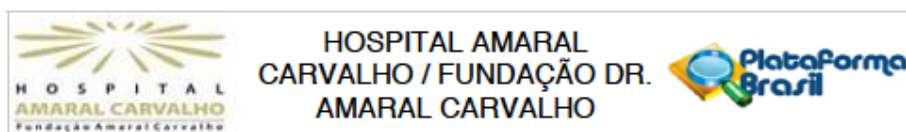
PARECER CONSUBSTANCIADO DO CEP

DADOS DO PROJETO DE PESQUISA

Título da Pesquisa: FLIM (Fluorescence Lifetime Imaging Microscopy): uma nova ferramenta para diferenciação de lesões clinicamente semelhantes

Pesquisador: ANA GABRIELA SALVIO

Área Temática:

Versão: 3

CAAE: 71208817.5.0000.5434

Instituição Proponente: FUNDACAO DOUTOR AMARAL CARVALHO

Patrocinador Principal: UNIVERSIDADE DE SAO PAULO

DADOS DO PARECER

Número do Parecer: 2.568.603

Apresentação do Projeto:

O estudo FLIM (Fluorescence Lifetime Imaging Microscopy): uma nova ferramenta para diferenciação de lesões clinicamente semelhantes, por microscopia de tempo de vida de fluorescência.

Objetivo da Pesquisa:

Nao se aplica à presente avaliação.

Avaliação dos Riscos e Benefícios:

Nao se aplica à presente avaliação.

Comentários e Considerações sobre a Pesquisa:

O estudo foi apresentado a esse CEP e também ao CONEP. As considerações feitas foram objeto de modificações e adequações, por parte dos responsáveis.

Considerações sobre os Termos de apresentação obrigatória:

De acordo com as recomendações. Há, porém, na pagina da Plataforma Brasil, a permanência do texto de Informações Básicas que , smj, é o original e que foi objeto das recomendações citadas.Para que não haja prejuízo nas discussões no colegiado, o novo texto com as adequações, está presente na Plataforma.

Recomendações:

Se tecnicamente possivel, adequar o texto de informações básicas, com as correções e adequações

Endereço: Rua das Palmeiras, 89
Bairro: VILA ASSIS **CEP:** 17.210-120
UF: SP **Município:** JAU
Telefone: (14)3602-1194 **Fax:** (14)3602-1207 **E-mail:** cep.aurea@amaralcarvalho.org.br

Página 01 de 04
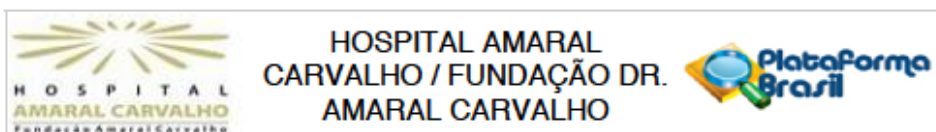
Continuação do Parecer: 2.568.603

citadas.

Conclusões ou Pendências e Lista de Inadequações:
Se tecnicamente possível, adequar o texto de informações básicas, com as correções e adequações citadas.

Considerações Finais a critério do CEP:
O colegiado acompanha o parecer do relator.

Informamos que nenhum dos pesquisadores envolvidos no estudo participou da votação.

Aproveito para recordar-lhe do compromisso de enviar Relatórios Semestrais referentes à evolução do estudo e Relatório Final contendo os resultados da pesquisa.

Qualquer alteração/emenda o projeto deverá passar novamente por apreciação deste Comitê de Ética em Pesquisa.

Não autorizamos divulgação dos dados e/ou publicação sem antes passar para análise deste CEP o Relatório Final de encerramento do estudo contendo os resultados da pesquisa.

ANTES DE INICIAR A PESQUISA É OBRIGATÓRIO QUE OS PESQUISADORES QUE ENTRARÃO NO HOSPITAL PARA COLETA DE DADOS ENTRE EM CONTATO COM O COMITÊ DE ÉTICA PELO TELEFONE (14) 36021194 EM PESQUISA PARA PROVIDENCIAR A DOCUMENTAÇÃO NECESSÁRIA E CRACHÁ DE IDENTIFICAÇÃO.

Este parecer foi elaborado baseado nos documentos abaixo relacionados:

| Tipo Documento	Arquivo	Postagem	Autor	Situação
Informações Básicas do Projeto	PB_INFORMAÇÕES_BÁSICAS_DO_PROJETO_909763.pdf	09/03/2018 16:12:09		Aceito
Projeto Detalhado / Brochura Investigador	CEP_FLIM_adequado.pdf	09/03/2018 16:11:53	GABRIEL ALMEIDA FERRACINI	Aceito
TCLE / Termos de	TCLEadequado.docx	09/03/2018	GABRIEL ALMEIDA	Aceito

Endereço: Rua das Palmeiras, 89
Bairro: VILA ASSIS   CEP: 17.210-120
UF: SP   Município: JAU
Telefone: (14)3602-1194   Fax: (14)3602-1207   E-mail: cep.aurea@amaralcarvalho.org.br

HOSPITAL AMARAL CARVALHO / FUNDAÇÃO DR. AMARAL CARVALHO
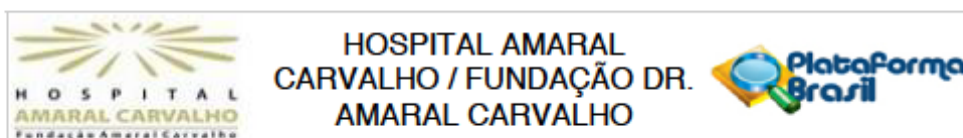
Continuação do Parecer: 2.568.603

Assentimento / Justificativa de Ausência	TCLEadequado.docx	16:08:35	FERRACINI	Aceito
Folha de Rosto	folha_de_rosto.pdf	09/03/2018 16:08:26	GABRIEL ALMEIDA FERRACINI	Aceito
Outros	Carta_CEP_DraGabriela.pdf	24/10/2017 15:14:35	GABRIEL ALMEIDA FERRACINI	Aceito
Projeto Detalhado / Brochura Investigador	CEP_FLIM_out_2017.docx	24/10/2017 15:11:41	GABRIEL ALMEIDA FERRACINI	Aceito
Outros	Termo_confidencialidade.pdf	10/07/2017 07:38:37	GABRIEL ALMEIDA FERRACINI	Aceito
TCLE / Termos de Assentimento / Justificativa de Ausência	TCLEv28042017.pdf	10/07/2017 07:38:25	GABRIEL ALMEIDA FERRACINI	Aceito
Outros	CV_DraAnaGabriela.pdf	10/07/2017 07:38:02	GABRIEL ALMEIDA FERRACINI	Aceito
Outros	Autorizacao_chefe_servico.pdf	10/07/2017 07:37:48	GABRIEL ALMEIDA FERRACINI	Aceito
TCLE / Termos de Assentimento / Justificativa de Ausência	10TCLEv28042017.pdf	24/05/2017 10:39:30	ANA GABRIELA SALVIO	Aceito
Declaração de Pesquisadores	8TermodeCompromissoRelatorioFinal.pdf	24/05/2017 10:38:15	ANA GABRIELA SALVIO	Aceito
Projeto Detalhado / Brochura Investigador	CVAGS.pdf	24/05/2017 10:37:26	ANA GABRIELA SALVIO	Aceito
Projeto Detalhado / Brochura Investigador	CVNMI.pdf	24/05/2017 10:31:56	ANA GABRIELA SALVIO	Aceito
Projeto Detalhado / Brochura Investigador	CVKurachi.pdf	24/05/2017 10:30:32	ANA GABRIELA SALVIO	Aceito
Projeto Detalhado / Brochura Investigador	CVRamon.pdf	24/05/2017 10:27:13	ANA GABRIELA SALVIO	Aceito
Declaração de Pesquisadores	6TermodeConfidencialidade.pdf	24/05/2017 10:25:32	ANA GABRIELA SALVIO	Aceito
Declaração de Pesquisadores	5DeclaracaodeOnusFinanceiro.pdf	24/05/2017 10:24:40	ANA GABRIELA SALVIO	Aceito
Declaração de Pesquisadores	2OficioCEP.pdf	24/05/2017 10:22:01	ANA GABRIELA SALVIO	Aceito
Declaração de Pesquisadores	1OficioDDS.pdf	24/05/2017 10:21:13	ANA GABRIELA SALVIO	Aceito
TCLE / Termos de	TCLEv28042017.docx	09/05/2017	ANA GABRIELA	Aceito

HOSPITAL AMARAL CARVALHO / FUNDAÇÃO DR. AMARAL CARVALHO
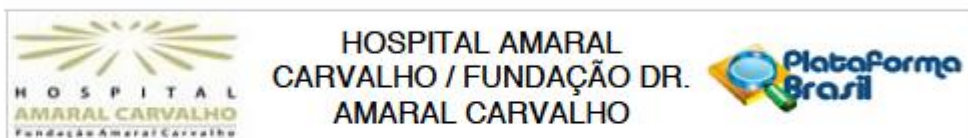
Continuação do Parecer: 2.568.603

Assentimento / Justificativa de Ausência	TCLEv28042017.docx	16:54:14	SALVIO	Aceito
Projeto Detalhado / Brochura Investigador	PPRamonv28042017.docx	02/05/2017 15:40:40	ANA GABRIELA SALVIO	Aceito

Situação do Parecer:
Aprovado

Necessita Apreciação da CONEP:
Não

JAU, 28 de Março de 2018

_____

Assinado por:
Osvaldo Contador Junior
(Coordenador)